2007

Fabrication and Study of ZnO Micro- and Nanostructures

Monica Morales-Masis
Wright State University

Fabrication and Study of ZnO Micro- and Nanostructures

A thesis submitted in partial fulfillment

of the requirements for the degree of

Master of Science

By

Mónica Morales Masís

B.Sc., Universidad de Costa Rica, 2005

June 7, 2007

Wright State University

Dayton-Ohio

WRIGHT STATE UNIVERSITY

SCHOOL OF GRADUATE STUDIES

June 7, 2007

I HEREBY RECOMMEND THAT THE THESIS PREPARED UNDER MY SUPERVISION BY Mónica Morales-Masís, ENTITLED Fabrication and Study of ZnO Micro- and Nanostructures BE ACCEPTED IN PARTIAL FULFILLMENT OF THE REQUIREMENTS FOR THE DEGREE OF Master of Science.

Gary Farlow, Ph.D.

Thesis Director

Lok Lew Yan Voon, Ph.D.

Department Chair

Committee on

Final Examination

Gary Farlow, Ph.D.

David C. Look, Ph.D.

Lok Lew Yan Voon, Ph.D.

Joseph F. Thomas, Jr., Ph.D.

Dean, School of Graduate Studies

ABSTRACT

Morales-Masís, Mónica. M.S., Department of Physics, Wright State University, 2007. Fabrication and Study of ZnO Micro- and Nanostructures.

ZnO micro-structures and nano-structures have been grown on two types of substrate by reacting condensed Zn vapor with oxygen. The source material was either pure zinc powder or zinc acetate which was either evaporated or decomposed. This was done in the temperature range 500 °C to 650 °C, in a flowing Ar plus oxygen ambient at atmospheric pressure. Variations in the carrier gas composition, gas flow rate and the position of the substrate in the furnace were found to control the formation and the morphology of the nanostructures. Scanning electron microscopy images of samples grown from a Zn powder source show forested needles approximately 100 nm in diameter by 1 μm long, and faceted rods from 500 nm to 700 nm thick. Samples grown from Zn acetate show the formation of nano crystals (from $\sim$ 100nm to $\sim$300nm) dispersed across the substrates. Photoluminescence measurements at 4.2K show a dominant line at $\sim$3.36 eV with additional features at 3.32 and 3.37 eV. The line widths are $\sim$3.5 meV indicating good quality material. The usual green-band emission is also observed. Hall measurements and CV profiling were attempted but they were unsuccessful due to the inability to make good contacts.

Contents

List of Figures

List of Tables

Acknowledgments

I would like to thank all the people who provided supervision, assistance and support during the course of my research.

I would like to thank my advisor, Dr. Gary Farlow, for his guidance, patience and interest in my work. Special thanks also go to Dr. David Look for including me in his research group and all his encouragement and support. Thanks to Dr. Bruce Claflin for providing SEM images and Wally Rice for the photoluminescence measurements.

I am forever grateful to Prof. Lok for giving me the opportunity to come to Wright State University; for all his help, assistance and support.

I want to thank my classmates and friends, especially Kineshma Munbodh, Gian Guzman-Verri and Dimitris Dakopoulos, for being there from the first day until the end of my master's program.

And finally, thanks to my family whose love and support have been always felt, even across the miles.

This work has been made possible by financial support from NSF GOALI Grant DMR0513968.

Chapter 1

Introduction

In the group of II-VI compound semiconductors, ZnO has received intense attention due to its remarkable combination of physical and optical properties. Its wide band gap (3.37 eV at room temperature), high exciton binding energy (60 meV), and its diverse growth morphologies, make ZnO a key material in the fields of nanotechnology and wide band-gap semiconductors.

One of the potential uses of ZnO is the fabrication of short wavelength devices, operating in the blue and ultra-violet regions of the electromagnetic spectrum, such as light emitting diodes, laser diodes and detectors. The principal advantage is that ZnO possesses a larger exciton binding energy than that of GaN (the current material used for optoelectronics in this wavelength range), which will allow devices operating with higher efficiency and lower power threshold for lasing by optical pumping at room temperature. Another of the important advantages is the ability to grow ZnO with relatively low cost, and ease. High quality GaN is very difficult to achieve.

With the reduction in size to the nanometer scale, ZnO structures have also shown novel properties. One of these properties is the quantum confinement effect which is observed as a shift in the band edges of the semiconductor. Consequently, a shorter wavelength of the emitted light is observed when the material is excited [1]. This

property is useful for the fabrication of UV light emitting devices from ZnO. The piezoelectric effect (conversion of a mechanical vibration into an electronic signal or vice versa) has also been experimentally measured for both nanobelts and bulk ZnO [2] showing that the effective piezoelectric coefficient is much larger for the nanobelts than that for bulk ZnO. This makes ZnO nanobelts useful for nanoresonators, nanosensors and nanoactuators which use the piezoelectric effect. Surface effects also become more significant with reduction in size. In particular ZnO nanostructures present their chemically sensitive surfaces in larger proportion than is the case for bulk samples which makes the nanostructures better sensors, and thus more useful in the fabrication of chemical sensors [2].

The high performance of the nanostructures has kept researchers interested in the synthesis, characterization, and fabrication of nanodevices. As a consequence, many techniques such as Molecular Beam Epitaxy (MBE) [3], Chemical Vapor Deposition (CVD) [4], thermal evaporation [2], electrodeposition [5], and sol-gel synthesis [6] have been developed to synthesize nano-structures; sometimes with well controlled size, shape and spatial distribution on the substrates.

Even though ZnO has been extensively studied, there is still much to be explored and understood about this material before fabricating commercial devices. 'p-type' doping in ZnO thin films has been reported using Li and N [7] and the group V dopants N, P, As and Sb [8, 9]. Routine p-type doping is one of the remaining issues, as is a reasonably complete understanding of the defect structure of bulk and nanostructured ZnO. The routine production of p-type ZnO would be a great advancement in optoelectronics and nanoelectronics allowing for the creation of p-n junction diodes involving homojunction ZnO. The obvious application consists of ZnO light emitting diodes (LED).

The purposes of this project is to grow ZnO micro- and nanostructures using an atmospheric pressure and low temperature technique, to observe the growth mor-

phology and characterize the parameters for optimum growth, and to characterize the photoluminescence and carrier concentration of the as-grown structures.

These have been achieved by growing ZnO using variations on the vapor phase process, which has been reported as one of the simplest and most useful techniques because of its economic accessibility and the variety of morphologies that can be obtained by variation of the growth parameters. ZnO structures were grown in the range from 500 to 650 °C using two different substrates, two different source materials, and a variety of gas flow rates. The synthesis and the proposed growth mechanism are explained in Chapter 3.

The structure of the final products were analyzed by scanning electron microscopy (SEM) and the various shapes were analyzed by consideration of crystal growth kinetics. This analysis confirmed the primary influence of the zinc vapor concentration (supersaturation) as well as the role of the surface energies of particular planes in the formation of the structures. It was not possible to achieve self organized nucleation.

The ZnO micro- and nanostructures were also examined by low temperature photoluminescence (PL). This confirmed the quality of the structures grown and gave insight into their defect structure. Photoluminescence is one of the basic research tools for optical characterization of materials. Its advantages are the sensitivity and simplicity of the data collection. However, one of its disadvantages is the increased remoteness of the raw data from the physical phenomena of interest. Thus, considerable analysis is then required to infer the origin(s) of the observed radiation.

The PL spectra were measured by collaborators at Wright-Patterson Air Force Base. Chapter 4 presents a description of the PL spectra acquisition and an analysis of the PL spectra obtained from the ZnO micro- and nanostructures. These spectra are compared with results from a literature review of reported PL data for bulk and nanosize ZnO. Light emission, doping of the material, size, material quality and band structure are some of the features that have been inferred by various authors from

the PL spectra.

Knowledge of electrical properties are crucial as a complement to optical characterization for future applications in nanoscale electronics, photonics and device manufacture. Many electrical characterization techniques have been used, such as Hall effect measurements, deep level transient spectroscopy (DLTS) and capacitance-voltage profiling [9, 10]. These techniques are invaluable for providing information about the carriers or defects states within the semiconductor. In an effort to electrically characterize the samples grown for this study, the electrochemical capacitance voltage technique has been used. Chapter 5 will give a description of this technique, the experimental setup, and measurements on bulk ZnO. However, difficulties were encountered in the measurement of thin and non-uniform samples because of poor contact formation. Hall measurements were also attempted on the as-prepared ZnO but were unsuccessful, presumably because the depositions were not continuous.

Finally, in chapter 6, conclusions are drawn regarding growth, optical and electrical characterization of ZnO from bulk and micro-/nanostructures. The results of this project have led to a better understanding of the growth of ZnO structures and their optical properties, which could be important for the fabrication of future ZnO based devices.

Chapter 2

Background

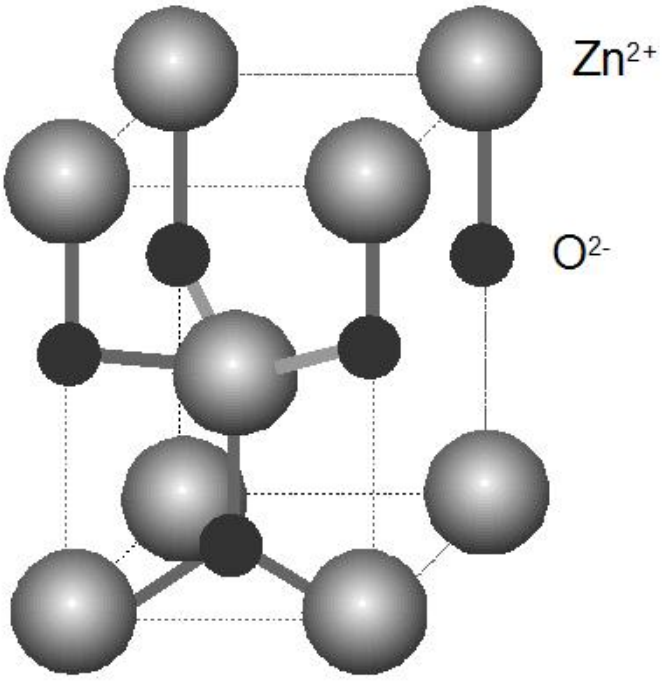

Figure 2.1: Unit cell of wurtzite structure ZnO

2.1 Physical Properties of ZnO

The basic physical properties of ZnO are summarized in Table 2.1, based on recently reported data on bulk ZnO [11].

Table 2.1: **Physical properties of ZnO.** *Adapted from Ref [11] except as noted.*

Properties	Value
Crystal structure	wurtzite (stable phase at 300 K)
	zinc blende
	rocksalt
Lattice parameters (at 300K)	
a_0	0.32495 nm
c_0	0.52069 nm
c_0/a_0	1.602
Energy gap	3.37 eV (at 300 K), direct [2]
	3.4376 eV (at 4.2 K) [12]
Density	5.606 g/cm^3
Melting point	1975 °C
Exciton binding energy	60 meV
Electron effective mass	0.24
Electron Hall mobility at 300 K	
for low n-type conductivity	200 cm^2/Vs
Hole effective mass	0.59
Hole Hall mobility at 300 K	
for low p-type conductivity	5-50 cm^2/Vs
Typical impurities	H, Al, In, Ga
Typical defects	Zinc interstitials
	Oxygen vacancies
	Zinc vacancies
	Complexes

2.1.1 Crystal structure

ZnO crystallizes in the Wurtzite structure at room temperature and ambient pressure (Fig. 2.1). It has a hexagonal lattice, characterized by two interpenetrating hexagonal-close-packed (hcp) sublattices of Zn^{+2} and O^{-2}. The lattice parameters of the unit cell have a c/a ratio of 1.602 which is 1.8 % off of the ideal hexagonal-close-packed structure of 1.633.

The zinc and oxygen ions are tetrahedrally coordinated, resulting in a non- centrosymmetric structure. The arrangement of the atoms in this structure gives rise to a net dipole moment, or polar symmetry, responsible for properties like piezoelectricity and spontaneous polarization.

The tetrahedral coordination is an indicator of covalent bonding (sp^3). However, the Zn-O bond also possesses a very strong ionic character, with an ionicity of f_i= 0.616 [13]. Thus, ZnO lies on the borderline between being classified as a covalent or ionic compound.

Other metastable forms of ZnO are zinc blende and rocksalt [14].

2.1.2 Doping of ZnO

One of the big challenges in ZnO research is the doping of the material. ZnO occurs naturally as n-type with reported concentrations from $\sim 10^{16}$ to 10^{18}cm^{-3} in typical high-quality material [15]. The origin of the n-type conductivity is controversial in both theoretical and experimental studies. From photoluminescence and annealing experiments, D. C. Look et al. [15] have concluded that group-III elements (Al and Ga) are the most prevalent donors in ZnO. H can also be present and is believed to be the shallower donor. C. G. Van de Walle [16] also assigned H as one of the principal candidates for the n-type dopant based on first principles, density-functional calculations. C. G. Van de Walle shows that the hydrogen occurs exclusively in the positive charge state, thus, it always acts as a donor in ZnO. Native defects (O vacancies and Zn interstitials) have also been suggested as possible n-type dopants. S. B. Zhang, using theoretical calculations [17], reported n-type doping due to zinc interstitials. Since the zinc interstitial is in a shallow level, it supplies electrons, and this, together with its low formation energy, allows the abundance of this defect. On the other hand, native defects that could compensate the n-type doping have high formations energies under zinc-rich growth conditions so the presence of "electron

killers" would be rare. The oxygen vacancy (V_0) has been found to be a deep donor [15, 17], and it is unlikely to be responsible for free-electrons concentrations of the order of 10^{17} cm^{-3} or higher.

Different levels of n-type doping and p-type doping have proven extremely difficult to produce due to stability issues and compensation by low-energy native defects. Most of the attempts to produce p-type ZnO have employed N as the acceptor. Nitrogen is a natural choice for an acceptor dopant since it has about the same ionic radius as that of O, and thus it can be placed in a substitutional oxygen site [15]. The effort to produce p-type ZnO can also be affected by the presence of H, being a donor in ZnO by compensating the acceptors[18]. In addition to N_0 (Nitrogen on an oxygen site), other possible candidates for acceptors are P_0 (Phosphorus on an oxygen site) and As_0 (Arsenic on an oxygen site) and other group-V elements. Production of p-type ZnO using P and As has been experimentally successful [8]. Finally, from the group I elements, Li, Na, K on Zn sites are also candidates for p-type doping. One of the important results has been the fabrication of p-type ZnO thin film using two acceptors, Li and N; the film being a stable and low-resistivity material [7]. However, as for the group-V elements, more studies are necessary.

In the case of nanostructures, no reports on p-type ZnO were published until December 2006 when Xiang et al.[19] reported for the first time the synthesis of high-quality p-type ZnO nanowires. These were grown using the chemical vapor deposition method with phosphorus pentoxide as the dopant source, and a mixture of ZnO, zinc and graphite powders.

The bulk production of high quality p-type ZnO would open great opportunities for the fabrication of ZnO-based UV diode devices.

2.1.3 Applications

Due to interest in the material, high quality bulk and epitaxial ZnO as well as novel ZnO nanostructures have been synthesized by means of simple and accessible methods. This opens the door to the fabrication of novel devices for use in optoelectronics and nanoelectronics, and as sensors, detectors and switches [2]. In this section, a brief overview of the most recent devices and applications of ZnO will be reviewed.

One of the devices with the greatest potential for commercial impact is a light emitting diode (LED) in the UV region. The production of thin-film-based UV LEDs has already been successful [8]. An example is the report from Ryu et al.[20] of the fabrication of a ultraviolet laser diode based on layered ZnO/BeZnO films which were pressed to form a multiple quantum well (MQW). The n-type layers were Ga-doped ZnO/BeZnO films and As-doped ZnO/BeZnO films as p-type layers. More recently, the same group also demonstrated the fabrication of a ZnO UV/visible LED [21] by combining a UV LED with phosphors to produce light covering the whole visible color spectrum.

At the nanoscale, the fabrication of p-type ZnO nanowires has been possible [19]. 'p'-type doping, together with the growth of vertical arrays of nanowires, enables the fabrication of LEDs with a large junction area, which in turn translates to higher efficiency. Lasers based on the cylindrical geometry nanowires could also serve as high-efficiency light sources for optical data storage and imaging.

A ZnO based field effect transistor (FET) has been made using single nanobelts [22, 23]. The principle of this device is that controlling the gate voltage would control the current flowing from the source to the drain. The production of these FETs using nanobelts has allowed the exploration of physical and chemical properties of the nanostructures. Arnold et al. [23] has demonstrated the fabrication of nanoscale FETs using SnO_2 and ZnO nanobelts as the FET channels. The reported values for a ZnO FET showed a gate threshold voltage of -15 V, a switching ratio I(ON)/I(OFF)

of nearly 100, and a peak conductance of 1.25×10^{-3} $(\Omega\text{cm})^{-1}$. It was also demonstrated that the ZnO nanobelt FETs are sensitive to UV light showing an increase in conductivity due to the photogeneration of electron-hole pairs or UV induced surface desorption [2, 23]. This treatment provides a way of tuning the electrical performance of the nanobelt devices.

ZnO also presents suitable characteristics useful in the development of gas sensing devices (metal oxide sensors, NO_2, CO, H_2, NH_3)[2]. A recent report is the fabrication of a low-temperature hydrogen sensor based on Au nanoclusters and ZnO films [24]. Moreover, Moreira et al. have shown with numerical calculations and experiments the good sensitivity of ZnO to the mass loading effect through a high electromechanical coupling coefficient and temperature compensation [25]. Because ZnO is a bio-safe and biocompatible material, it can be used for biomedical applications. Nanosensors based on nanobelts have the potential for implantation in biological systems and may be unique in detecting single cancer cells and measuring pressure in a biological fluid [2].

Finally, the piezoelectricity of ZnO leads to the fabrication of vibrational sensors; nanoresonators which can be used to control the tip movement in scanning probe microscopy; nanogenerators, which can be used in the construction of wireless sensors, implantable biomedical devices and portable electronics. In a report in $Science, Vol.$ 312, Wang and Song [26] have demonstrated an approach to converting mechanical energy into electric power using aligned ZnO nanowires. These piezo-based nanogenerators have the potential of converting mechanical, vibrational, or hydraulic energy into electricity and powering nanodevices.

2.2 Growth Under the Vapor Phase Synthesis

In this study, the synthesis of ZnO is conducted by vapor phase synthesis in a horizontal quartz-tube furnace where the temperature, evaporation time, gas composition, and gas flow can be controlled. Vapor Phase Synthesis consists of the deposition of a vaporized material onto a solid substrate. In this work the source material is evaporated or decomposed from the melt, thus raising its partial pressure in the carrier gas flowing in the furnace tube. The vapor is condensed onto a solid substrate which then reacts with oxygen in the carrier gas flowing through the furnace tube. The substrate is located in a zone of lower temperature or facing the source material.

The Vapor Phase technique can be classified in different categories such as the Self Catalyzed Vapor Solid (VS), the catalyst assisted Vapor Liquid Solid (VLS) and Vapor Phase Transport (VPT), which are all based on the Vapor Phase technique but differ in the nucleation and growth mechanisms of the solid from the vapor species on the substrate.

Catalyst-assisted Vapor-liquid-solid method (VLS)

In this method, the vapor species are generated and then condensed into a metal drop which acts as a catalyst for the growth. After the precipitation of a liquid drop onto the substrate, the nucleation and the growth of the oxide follows. For ZnO, the morphology of the nucleated growth is generally wire or rod shaped. The diameter of the nanowires is controlled by the size of the liquid catalyst droplets (smaller catalyst yield thinner nanowires). Nanowires and nanorods produced by this method are remarkable for the uniformity of their diameter [27].

Self-catalyzed vapor-liquid-solid method (VLS)

In contrast to the catalyst-assisted process, this technique is a catalyst-free method, during which the nanostructures are produced by condensing directly from the vapor

phase. Because of that, morphology and alignment of the nanostructures are less controlled compared to the method before, in which the diameter of the nanowires is controlled by the size of the catalyst. However, it has been reported that under this synthesis more varied morphologies are possible due to the absence of constraints by the catalyst. Also, the technique has the advantage that contamination from the catalyst can be avoided during the growth process [27].

Vapor phase transport (VPT)

This process can be catalyst free or catalyst assisted (VS or VLS). However, the difference from the other techniques is that it requires a temperature gradient between the source material and the substrate. In this process vapor species are transported by the carrier gas flowing through the horizontal tube furnace, and then condensed onto the surface of the substrate placed in the zone of lower temperature. The temperature gradient between the source material and the substrate as well as the gas flow need to be carefully controlled in order to get good results.

2.3 Optical Characterization

2.3.1 Photoluminescence theory

Photoluminescence (PL) is the spontaneous (as opposed to stimulated) emission of light from a material under optical excitation.

In photoluminescence the material is irradiated with light of energy higher than that of the band gap. The photo-excitation causes electrons in the material to move into permissible excited states. When these electrons return to their equilibrium states, the excess energy is released by emission of light. The PL spectrum gives information about the transition energies between the various states which become occupied by excited electrons and thus is used to determine electronic energy levels.

The intensity gives a measure of the relative rates of radiative and non-radiative recombination processes.

The PL process can be summarized by the following steps [28]:

1. Electron-hole pairs are created by absorption of the exciting light.

2. Electron-hole pairs recombine radiatively.

3. Recombination radiation escapes from the sample.

Photoluminescence spectroscopy is a convenient characterization technique because it is nondestructive, contactless and results from simple spectral data collection. Although PL can be used to study different types of surfaces, conductive or non-conductive materials in any environment, it does depend on temperature. For high spectral resolution, liquid helium temperatures are required, but temperature dependent measurements can also be made for different purposes. Parameters like temperature and applied voltage can vary the PL intensity, allowing a further characterization of the electronic states and bands.

PL is very sensitive to discrete electronic states which most of the time are near the surface or interfaces of the material into which the exciting light can penetrate and from which the luminescence can escape. Thus, PL is a good tool for characterization of semiconductors: identifying band gap, impurity levels, excitonic states and the material quality of a sample [28, 29].

2.3.2 Photoluminescence analysis and recombination processes

In the emission of radiation, an electron in an excited state or higher energy makes a transition to an empty lower-energy state, emitting electromagnetic radiation with energy defined by the difference between the two states. The emission is expressed as the rate of photon generation per unit volume [29]. The radiation rate is determined

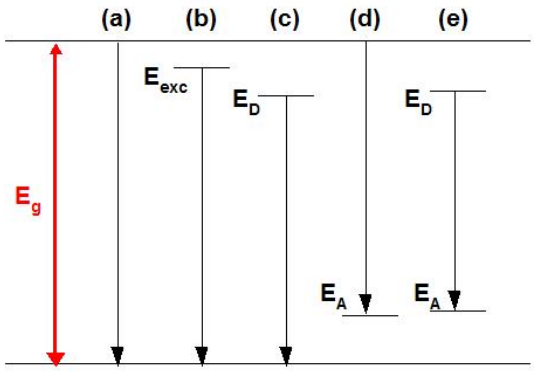

Figure 2.2: Schematic diagram of radiative transitions in semiconductors: (a) band to band, (b) exciton recombination, (c) donor to free hole transition, (d) free electron to acceptor transition, (e) donor-acceptor pair transition

by:

$$R = n_u n_l P_{ul},$$

where n_u is the density of carriers in the upper state, n_l the density of empty lower states, and P_{ul} the probability for 1 carrier/cm^3 in the upper state to make a transition to 1 vacancy/cm^3 in the lower state.

Different types of radiative transitions can be observed in the PL spectrum, resulting from the different ways electron-hole pairs recombine in a semiconductor:

EXCITON RECOMBINATION

The exciton recombination process is illustrated in Fig.2.2 (b). Two types of exciton transition can be found:

1. **Free excitons**: In direct and indirect-gap semiconductors, if the material is very pure, the Coulomb attraction between the generated electrons and holes can bind them together into a quasi-hydrogenic exciton. The parts of the exciton then recombine emitting a photon. In a direct-gap semiconductor, at low temperature, the energy of the emitted photon is:

$$h\nu = E_g - E_x, \tag{2.1}$$

and considering all the series of excited states of an exciton, the free exciton emission should consist of a series of narrow lines occurring at $E_g - \frac{1}{n^2}E_{x1}$. In an indirect-gap semiconductor, a phonon has to be emitted in the transition due to momentum conservation for minimum energy transitions. Direct transitions can also lead to phonon emission. This is because the emitting center, or the electron itself, can scatter off a phonon in the process of transition. The interchange of energy with the phonon gas broadens the range of energies present in the light emission. Interaction with the LO phonon is favored in the transition in which case an emission spectrum can be replicated at several lower photon energies given by:

$$h\nu = E_g - E_x - mE_p, \tag{2.2}$$

with m the number of optical phonons per transition. As m increases, the weaker the emission line and lower transition probability [29].

2. **Bound Excitons**: Bound excitons are obtained in the presence of impurities. A bound exciton is an electron associated with a neutral acceptor (A^0X) or a hole associated with a neutral donor (D^0X). Therefore the emission spectrum resulting from the bound exciton recombination is characterized by narrow lines at a lower energy (sub-bandgap) than that of the free exciton (near bandgap energy).

   However, ionized bound excitons can also be found. They are produced when an electric field exerts a stronger force on the electron than the local forces binding the electron to an impurity. Then, the center is ionized and the carrier

is free to move in the appropriate band (free electrons in the conduction band for ionized donors, and free holes in the valence band for ionized acceptors).

CONDUCTION BAND TO VALENCE BAND TRANSITIONS

At high temperature and in less pure materials, excited electron hole pairs remain as free carriers in their respective band states. The free carriers can then recombine via a band to band transition. The transition is illustrated in Fig.2.2 (a).

BAND TO AN IMPURITY LEVEL TRANSITIONS

These transitions are classified as shallow transitions and deep transitions. A shallow transition occurs to neutralize ionized donors or acceptors, then, shallow impurities are those that are near the band edge. Deep transitions involve an electron in the conduction band combining with a neutral acceptor (Fig. 2.2 (d)) or a hole in the valence band combining with a neutral donor (Fig. 2.2 (c)).

Variations in the material over space give a small variation in the energy levels of the impurities so that these lines tend to be wider than exciton or band edge transitions.

The PL peak for this kind of transitions is located at:

Direct transitions:

$$h\nu = E_g - E_i \tag{2.3}$$

Indirect transitions:

$$h\nu = E_g - E_i - E_p \tag{2.4}$$

with E_i the energy of the impurity level and E_p the phonon energy.

The variation in E_i increases with the doping concentration, and a broadening of the PL peaks can be observed. For purer materials, exciton recombination may be more probable than the deep transition. The exciton recombination can be distinguished by its very narrow emission spectrum.

DONOR-ACCEPTOR TRANSITIONS

When the semiconductor contains both donors and acceptors, electron-hole pairs excited optically can be trapped at ionized donors (D^+) and acceptors (A^-) sites to produce neutral donors (D^o) and acceptors (A^o) centers. In returning to equilibrium, some electrons on neutral donors will recombine with holes on neutral acceptors giving place to a donor-acceptor pair transition (DAP).

The photon emitted will have energy,

$$h\nu = E_g - E_A - E_D + \frac{e^2}{4\pi\epsilon_0\epsilon R_{DA}} \tag{2.5}$$

with the last term the Coulomb interaction, which depends on the pair separation. The bigger the separation of the pair, smaller the Coulomb interaction and with it the lower photon energy. Then, the emission intensity should increase as the pair separation decreases reflecting the energy dependence of the transition matrix element. The donor acceptor transition is illustrated in Fig.2.2 (e).

QUANTUM CONFINEMENT EFFECT

Quantum confinement occurs in nanocrystals when their size is reduced so that it approaches the size of the Bohr exciton radius (the size of an exciton in bulk crystal).

Photoluminescence can be used to observe the quantum confinement effect in nanostructures. However, there are few reports on quantum confinement effect in ZnO nanostructures, most of these nanowires, rods or crystals with characteristic size

no larger than 10 nm to 15 nm [63]. Experimental evidence of quantum confinement effects have been reported by Gu et al. [63] who observes PL and adsorption spectra from nanorods of radius 1.1 ± 0.1 nm. Lu et al. [59, 1] have also observed the quantum size confinement effect in the PL spectra from quantum dots having radius as large as 6 nm. The nanodots studied by Lu et al. exhibit a strong free exciton adsorption at room temperature at 3.41 eV, significantly larger than that of bulk ZnO (3.37 eV), representing ∼90 meV blue-shift.

The as-prepared ZnO samples studied in this project present diameters of at least 90 to 100 nm. And as a consequence, no quantum confinement is expected nor observed at these dimensions.

Observation of highly resolved features from the PL system indicate that the practical resolution is 2 to 5 meV which would allow observation of quantum confinement effects if they occurred.

In conclusion, if the quantum confinement effect occurred we would be able to see it with the PL system, but since the structures are larger no quantum confinement effect is observed.

2.4 Electrical Characterization

The study of the electrical properties when combined with optical characterization provides fundamental information for future applications in the development of optoelectronic devices.

There are several methods for determining the carrier and doping concentration in a semiconductor. Among them are, capacitance-voltage (C-V), Hall effect, secondary ion mass spectrometry and spreading resistance.

For the purposes of this work, the electrochemical capacitance-voltage technique and Hall measurements were applied in an effort to characterise the carrier concentration mobility and doping levels in these samples.

2.4.1 Hall measurements

The Hall effect is widely used in characterizing the electrical properties of various materials. The technique measures carrier concentration and carrier mobility. Analysis of these data can provide information about donor or acceptor concentrations [30].

When a magnetic field is applied at right angles to a current flow, an electric field E_H is generated which is mutually perpendicular to the current I and magnetic field B, and which is directly proportional to the product of the current density and magnetic field. It is possible to define a Hall coefficient R_H by $R_H = E_H/JB$, with J the current density through the specimen and B the magnetic field. If there is only one type of carrier, the Hall coefficient R_H can be shown to be equal to $R_H = -r_n/ne$ or r_p/pe, with n or p the carrier concentration and r close to unity. Assuming that the conductivity σ is measured at the same time, then a Hall mobility can be defined as $\mu_H = R_H\sigma$. If there is mixed conduction the analysis is more complicated, but a mobility can be deduced from the Hall coefficient and the conductivity.

Hall measurements were attempted on the ZnO structures produced in our laboratory but gave inconsistent doping and carrier concentration values. Ultimately, it was not possible to establish adequate current to get a reliable current through the samples to get a reliable Hall voltage measurement.

2.4.2 Electrochemical capacitance-voltage (ECV) profiling technique

This technique consists of a C-V system combined with an electrochemical etching system which can be used to measure the electrical carrier concentration as function of depth in the semiconductor. To measure the carrier concentration by this method, the semiconductor has to be placed in contact with an electrolyte, and the conditions must be such that a region depleted of carriers is formed. The semiconductor electrolyte interface serves two functions:

- It behaves as a Schottky diode permitting the carrier concentration measurements.
- Via an electrochemical dissolution reaction, the surface material is removed up to several tenths microns at a controlled and calculable rate. Thus, the Schottky condition can be achieved as successively deeper layers of the sample. Successive C-V measurements will reveal the carrier concentration at successively deeper levels.

Capacitance-voltage profiling

In a Schottky barrier between a metal and a semiconductor, a depletion region is formed by the combined effect of the contact potential(Φ_0), and an applied bias (V). The electrostatic potential $\Phi(x)$ at any point of the depletion region is given by the Poisson's equation:

$$\frac{d^2\Phi}{dx^2} = \frac{-\rho(x)}{\epsilon\epsilon_0} \tag{2.6}$$

where $\rho(x)$ is the charge distribution as a function of depth, near the junction. Considering an n-type semiconductor, under the assumption of an uniformly doped

material and an abrupt cut off of n(x) (the electron density distribution at the edge of the depletion region w_d), the charge distribution is given by $\rho(x) = -qN_d$ at the depletion region [31], with N_d the bulk ionized donors. Then, the first integral of 2.6 gives the electric field within the depletion region. And integrating E, the solution of 2.6 is,

$$\Phi(x) = \frac{-qN_d(w_d - x)^2}{2\epsilon\epsilon_0} \tag{2.7}$$

in the region $0 < x < w_n$

At x=0, the potential is $\Phi = \Phi_0 - V = qN_d w_d^2/2\epsilon\epsilon_0$, from whence the expression for the depletion layer is obtained,

$$w_d = \left[\frac{2(\Phi_0 - V)\epsilon_0\epsilon}{qN_d}\right]^{\frac{1}{2}} \tag{2.8}$$

The differential capacitance of the depletion region is given by $C = AdQ_s/dV$ where Q is the semiconductor charge. The capacitance is determined by superimposing a small-amplitude ac voltage v on the dc bias voltage V. When the ac voltage increases from zero to a small positive voltage, it adds a charge increment dQ_m to the metal contact , and this increment has to be balanced by an equal semiconductor charge increment, given by $dQ_s = qN_d dw$. It is assumed that N_d does not vary over the distance dw. Replacing dQ_s on the expression for C and calculating dw_d/dV from 2.8, the differential capacitance is,

$$\begin{aligned} C &= A\left[\frac{qN_d\epsilon_0\epsilon}{2(\Phi_0 - V)}\right]^{\frac{1}{2}} \\ &= \frac{\epsilon\epsilon_0 A}{w_d} \end{aligned} \tag{2.9}$$

Differentiating 2.9 with respect to voltage gives the charge carrier density N_d (for

n-type) or N_a (for p-type) at the edge of the depletion layer:

$$\begin{aligned} N &= \frac{1}{q\epsilon_0\epsilon A^2}\frac{C^3}{dC/dV} \\ &= \frac{2}{q\epsilon_0\epsilon A^2(d(1/C^2)/dV)} \end{aligned} \tag{2.10}$$

Equations 2.8, 2.9 and 2.10 are the key equations for profiling of the doping level [32]. The doping level density will be obtained from a $C-V$ curve by taking the slope dC/dV or from a $1/C^2-V$ curve and by taking the slope $d(1/C^2)/dV$. The depth at which the doping density is evaluated is obtained from Eq. 2.8.

ECV Theory

The electrochemical capacitance-voltage (ECV) profiling technique is based on the measurement of the capacitance of an electrolyte-semiconductor Schottky contact at a constant dc bias voltage. In p-type semiconductors (holes as majority carriers) the carrier depletion condition is satisfied by biasing the sample negative to attract positive ions to the interface. The holes are repelled making a depletion layer (Fig.2.3 (a)). For an n-type semiconductor negative ions at the interface are required necessitating a positive bias on the semiconductor side of the interface (Fig.2.3 (b)).

Field penetration into the electrolyte is negligible providing the electrolyte is fairly concentrated (0.1M), in which case the semiconductor/electrolyte interface behaves as a Schottky junction. The equations for the depletion width (Eq. 2.8) and capacitance (Eq. 2.9) for a metal/semiconductor junction apply for such a system.

The depth profiling is achieved by electrolytically etching the semiconductor between capacitance measurements. For the etching of the material, the presence of holes is necessary in the semiconductor. In p-type material the etching is achieved by simply forward biasing the semiconductor/electrolyte junction which drive holes to

the interface. But in n-type material, holes have been supressed and an excess has to be created for the etching to take place. Excess Holes are created by illuminating the sample with light of higher energy than that of the band gap, promoting electrons from the valence band to the conduction band leaving holes behind. In this case, the etching takes place under conditions of reverse bias. These processes are shown in Fig.2.4.

The depth W_r to which the semiconductor is etched depends on the dissolution current I_{dis} according to the Faraday's law of electrolysis:

$$W_r = \frac{M}{ZF\rho A} c \int_0^t I_{dis}\, dt \tag{2.11}$$

with M the molecular weight, Z impedance, F Faraday constant (9.64x10^4 C), ρ density and c concentration. Because the carrier density is measured at the edge of the depletion layer, the corresponding depth is equal to the sum of the etch depth and the depletion depth $X = W_d + W_r$.

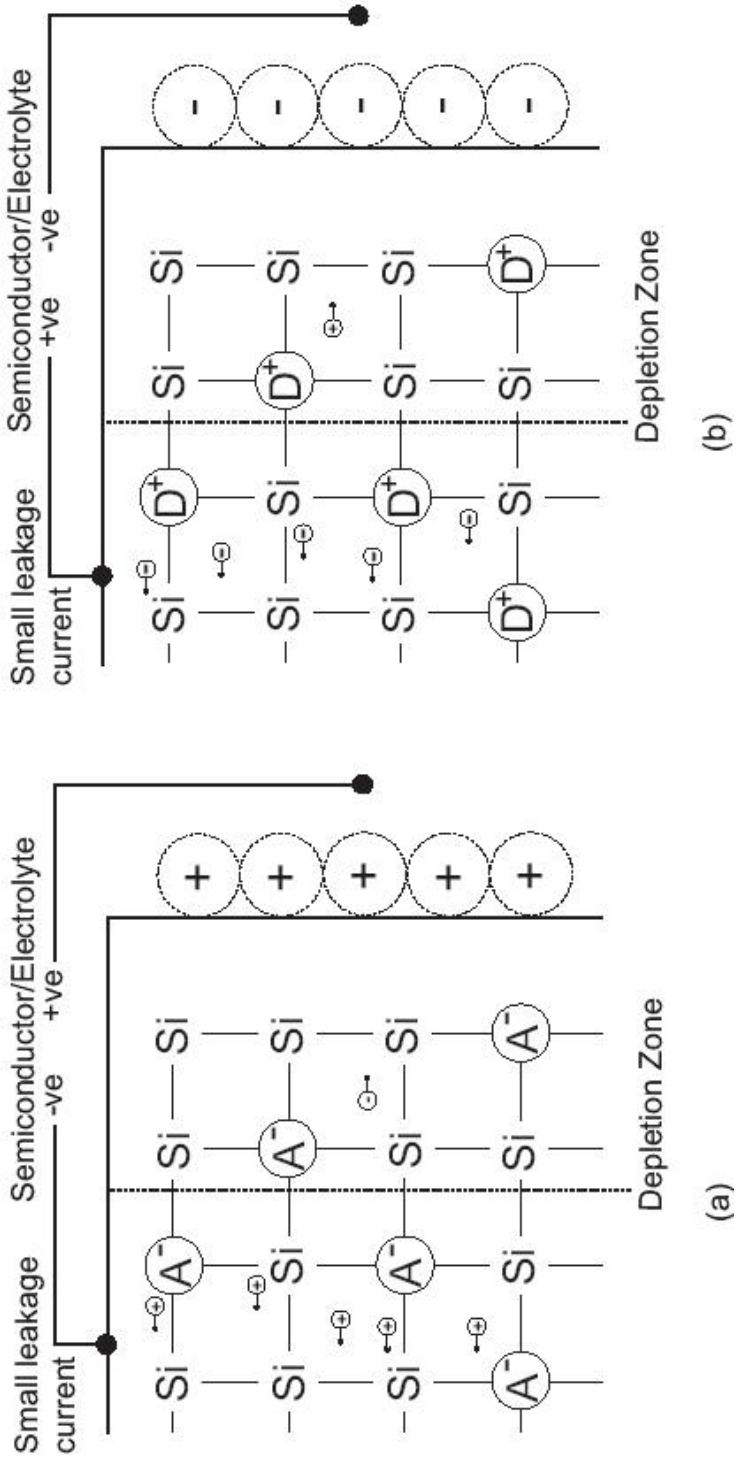

Figure 2.3: Depletion region in a (a) p-type and (b) n-type semiconductor

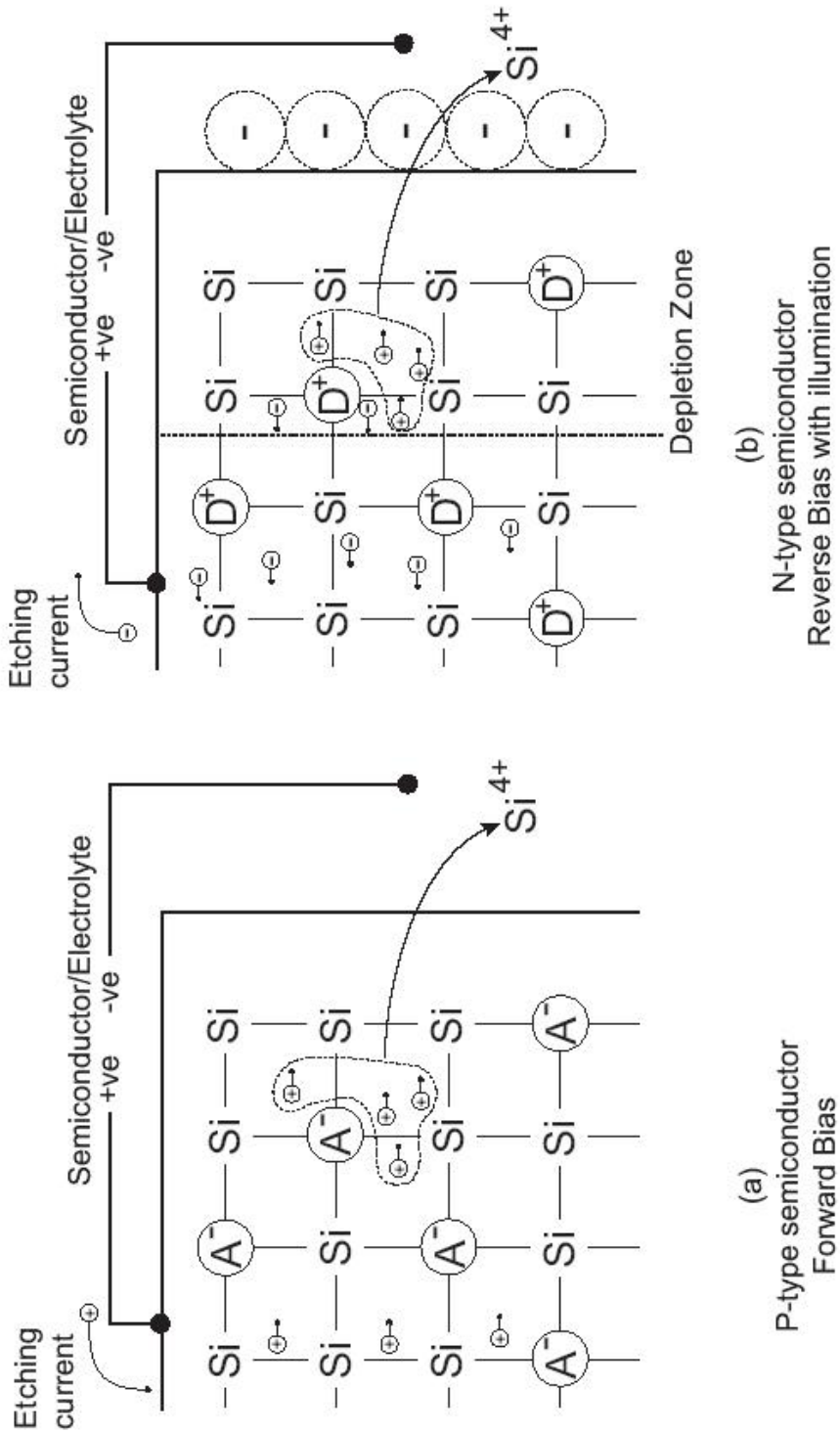

Figure 2.4: Etching process for n-type and p-type semiconductor materials

Chapter 3

Synthesis and Formation of ZnO Nanostructured Materials

The growth of ZnO films,and ZnO micro and nano-crystals has been extensively studied and many techniques have been developed looking for a better control in the size, shape and distribution of the ZnO structures. This implies knowledge of the influence of the experimental parameters on the kinetics and nucleation on the final morphology of the micro- and nano-structures. Our work is focused on a vapor-phase processes, this being a useful technique for its simplicity and accessibility and for the variety of morphologies that can be obtained with variations in the growth parameters [2]. The Vapor Phase Processes consists of the evaporation, sublimation or decomposition of a source material (Zn acetate or Zn powder in this work), followed by the condensation of the vapor onto a solid substrate, located in a zone of lower temperature and or higher pressure in a physical position where the substrate will block vapor flow. In this work, the synthesis is conducted in a horizontal quartz tube furnace with zoned control of temperature in which the temperature, evaporation time and gas flow is controlled.

Two different Vapor Phase processes have been used: 1) simple evaporation of

the source material which is deposited on a substrate placed face down in front of the source material (Self-catalyzed vapor liquid solid process), and 2) flowing gas transport of the vapor species resulting from the decomposition or evaporation into a zone of lower temperature where the material is deposited (Vapor Phase Transport Process). ZnO is believed to form from the oxidation of condensed metal.

3.1 Equipment and Materials

The ZnO samples were grown from zinc vapor reacted with flowing oxygen. This was performed in a horizontal tube furnace with a temperature and time controller (OMEGA CN-2010 Series Programmable Controllers). Using the Ramp and Soak function on the controller (the capability to control the temperature and its rate to change over a pre-determined time span) the system was programmed to either hold the temperature constant or ramp the temperature at a constant rate for a fixed period of time. The temperature gradient along the tube was measured using a separate thermocouple different from that monitoring the source material which could be moved freely along the length of the tube. A gas supply manifold for either N_2 plus O_2 or Ar plus O_2 was adapted to the tube. Each gas supply was equipped with a flow meter (Cole Parmer 32712) with a digital display and range between 0-100 sccm to control the amount of gas flowing through the tube. The combination of flow rates was used to control the ratio of Ar/O_2 or N_2/O_2 flow. The carrier gas flows from the left of the tube and leaves at the right side by bubbling through an Erlenmeyer flask filled with diffusion pump oil. This prevents atmospheric back flow and holds the pressure at 1 atm. A schematic representation of the equipment is presented in Fig. 3.1.

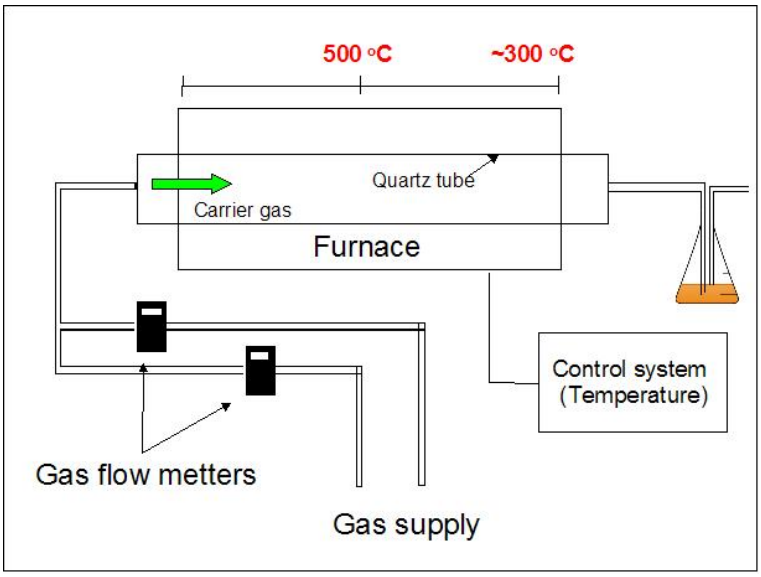

Figure 3.1: Schematic diagram of the experimental equipment for the growth of ZnO nanostructures

SOURCE MATERIALS: The materials used for the growing of ZnO are,

1. Zn powder 99.9 % and 99.9999 %

2. Zn powder, as in (1) but washed with HCl (0:1) and distilled water, and dried for $\sim$ 10 hours at 50 °C under an Argon or Nitrogen ambient, to remove oxide scale.

3. Zn acetate dihydrate.

SUBSTRATES: the substrates were chosen to favor c-axis growth of ZnO.

1. Sapphire (0001) Fig.3.2 shows the relation between ZnO(0001) grown on Sapphire (0001)

2. Silicon (111) Fig.3.3

CARRIER GAS:

1. Argon

2. Nitrogen

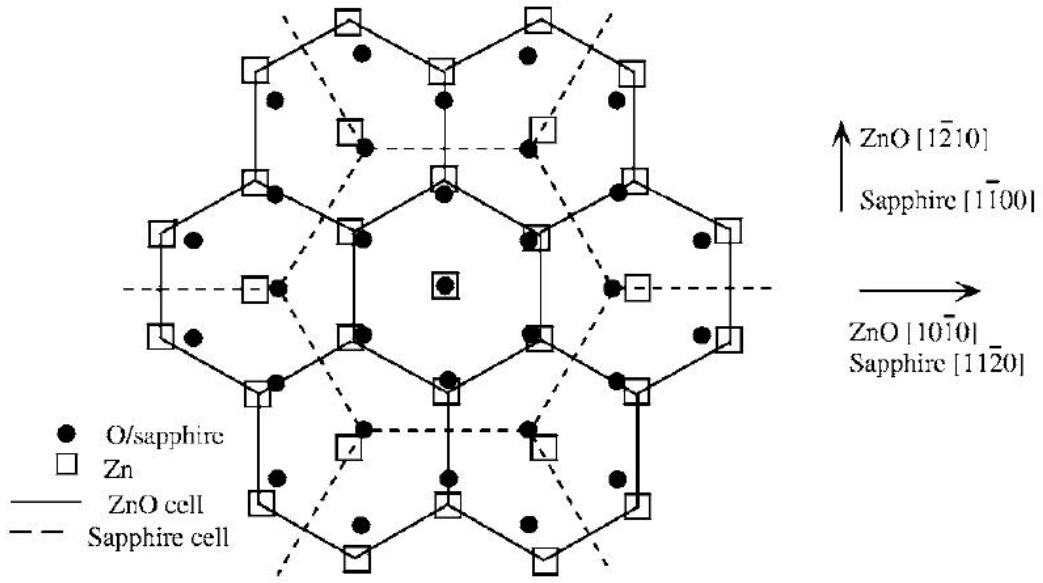

Figure 3.2: Representation of the epitaxial relationships of ZnO (0001) and Al_2O_3 (0001). Figure from Ref.[14]

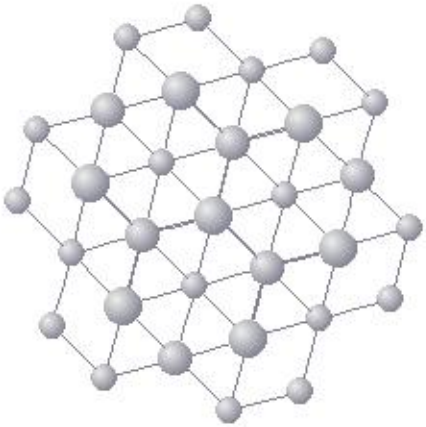

Figure 3.3: Plan view of the Si (111) plane where the ZnO structures were grown

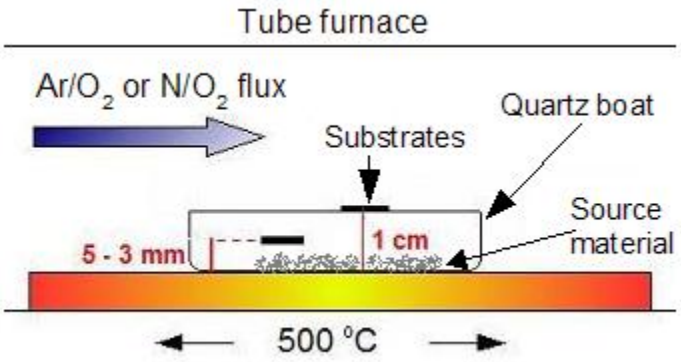

Figure 3.4: Schematic diagram of the quartz boat and vertical position of the substrates

3.2 Self-Catalyzed Vapor Liquid Solid Process (VLS)

In this process the source material (Zinc powder 99.9 % and 99.9999 %) is loaded in a quartz boat and placed at the center of the horizontal tube furnace. Argon gas or Nitrogen gas is flowing all the time through the tube. The temperature in the furnace is elevated at a rate of $\sim$ 20 °C/min until the center of the furnace reaches the desired temperature (500 °C, 525 °C or 600 to 650°C). The vaporization temperature of Zinc metal is 907 °C, then evaporation at these temperatures will be very slow. It is important that the evaporation rate is slow so that small features can be grown.

At that point, the oxygen flow is turned on. The substrates were placed above the source material at the vertical distances of 10mm, 5mm or 3mm (Fig. 3.4)

Due to the normal oxidation on the surface of the Zinc powder, it was found necessary for the source material to be washed with HCl (equation 3.1) followed by distilled water to leave bare Zinc in the boat. It was also dried for $\sim$7 to 10 hours in-situ to flush all the water produced in the reaction from the furnace tube. This procedure is believed to increase the volatility of the source material as it melts by eliminating oxide scale floating on the surface, and thus allowing growth at lower temperatures.

$$\mathrm{ZnO}(s) + 2\mathrm{HCl}(aq) \rightarrow \mathrm{ZnCl_2}(aq) + \mathrm{H_2}O(l) \tag{3.1}$$

When the temperature is above the melting point of Zn (419 $^{\circ}C$), the Zn melt partially evaporates under an Ar/O_2 or an N/O_2 ambient. The vapor species of Zn are then condensed onto the surface of the substrate placed face down above the source material at the vertical distances of 10mm, 5mm, or 3mm (See Fig.3.4). When the controller indicates the desired temperature at the center of the tube, the Oxygen starts flowing and the condensed droplets of Zinc will react with the oxygen, giving place to the nucleation and growth of the structures.

The chemical reaction of the Zinc droplets with the oxygen to form ZnO is,

$$\mathrm{Zn}(l) + \frac{1}{2}\mathrm{O_2}(g) \rightarrow \mathrm{ZnO}(s) \tag{3.2}$$

This reaction involves a change in the Gibbs energy of the system,$\Delta G = G_{\mathrm{products}} - G_{\mathrm{reactants}}$ or

$$\Delta G = G_{\mathrm{ZnO}} - (G_{\mathrm{Zn}} + \frac{1}{2}G_{\mathrm{O_2}}) \tag{3.3}$$

Using thermodynamics data [33], we can determine the change of the free energy in the reaction at 500 °C or 525 °C:

At 525 °C (798 K),

$$\Delta G = -398.324 + 42.140 + 172.901 = -183.283\mathrm{kJ/mol} \tag{3.4}$$

In order for nucleation to occur the total free energy of the system in the reaction must decrease, as is seen in the above calculation. The growth kinetics and nucleation will be explained in the last section of this chapter.

The morphology and size of the final products is expected to depend on a number

of factors, like the pressure inside the tube, the growth temperature, substrate, time and gas flow. Different values for the growth temperature, gas flow rates and vertical distance of the substrate from the source material were used in this study. From these, a variety of morphologies, as well as different sizes, were found. A representative set of examples is listed in Table 3.1.

Table 3.1: **Experimental parameters for morphologies of ZnO observed using the VLS process**

Source Material	Substrate	Temp. growth (°C)	Vertical distance (mm)	Growth time (min)	Gas Ar (sccm)	Flow O_2	Morphology
Zn powder	Si	500	10	60	100	25	nano-needles (Fig.3.5)
Zn washed	Al_2O_3	525	∼3	60	100	5	faceted rods (Fig.3.6(a))
with HCl	Al_2O_3	525	∼3	15	100	5	nano-crystals (Fig.3.6(b))
”	Al_2O_3	550	∼5	60	100	5	dense packed micro-rods
Zn powder	Si	650	10 ∼3	60	100	5	non uniform nano-structures over a thick ZnO matrix (Fig.3.7)
Zn powder	Si	500	10	60	250	60	thin film (Fig.3.5)

Growing under different carrier gas flow rates confirmed the fact that a high gas flow rate will influence the vapor concentration of zinc. A high flow of carrier gas will transport the vapor species away from the substrate surface placed near the source material and thus it will grow under lower supersaturation. As a consequence, smaller structures are formed as is seen in the SEM images of samples grown at 100 sccm Ar + 25 sccm O_2 (Fig. 3.5(a) and (b)) which are smaller compared with the structures grown at 100 sccm Ar + 5 sccm O_2 (Fig. 3.6).The vertical distance from the source material also seems to influence the morphology. The influence of the substrate does not seem to matter much.

On the other hand, the influence of temperature is also observed. Growing at temperatures between 600 to 700 °C, the production of ZnO is so high that after 30

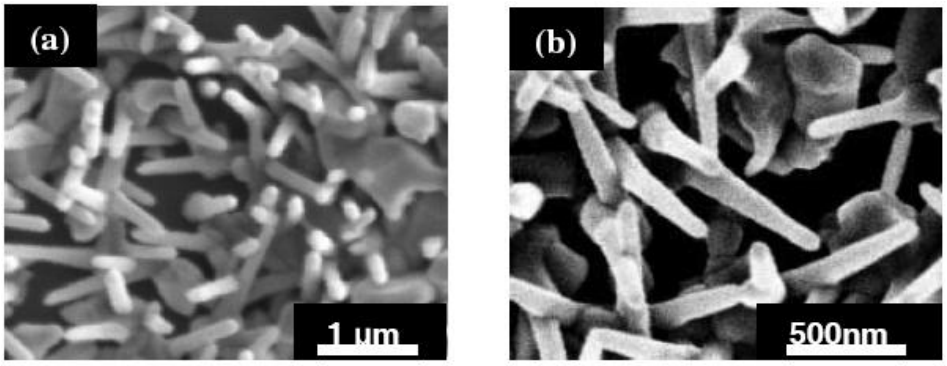

Figure 3.5: (a) SEM images of ZnO nano-needles randomly oriented grown on Si at 500 °C with 100 sccm of Ar flow and 25 sccm of O_2 flow. (b) Magnification of the needles showing a thickness of 90nm and 600nm long.

min. the tube is full of a white powder and the substrates are completely covered with a white thick layer. In this case two things are observed. One is the formation of a thick film on the substrate indicating fast growth and large features on the surfaces which serves as nucleation sites for the growth of thin and long wires, as shown in Fig 3.7. The second is the white powder which is consistent with reaction of Zinc and Oxygen in vapor phase and its subsequent precipitation. This is to be contrasted with the more dispersed structures observed at growth temperatures in the 500 to 600 °C range.

Other temperature parameters that affect the morphology are: 1) the temperature ramp rate as the desired growth temperature is approached which appears to affect the nucleation kinetics and the spatial uniformity of nucleated sites, 2) the actual growth temperature in the desired range of 500 to 600 °C which controls the amount of Zn in the vapor phase and thus the size of the nucleated ZnO features. The gas flow rate was also observed to affect the effective substrate surface temperature so the flow rate has to be monitored in conjunction with the substrate temperature.

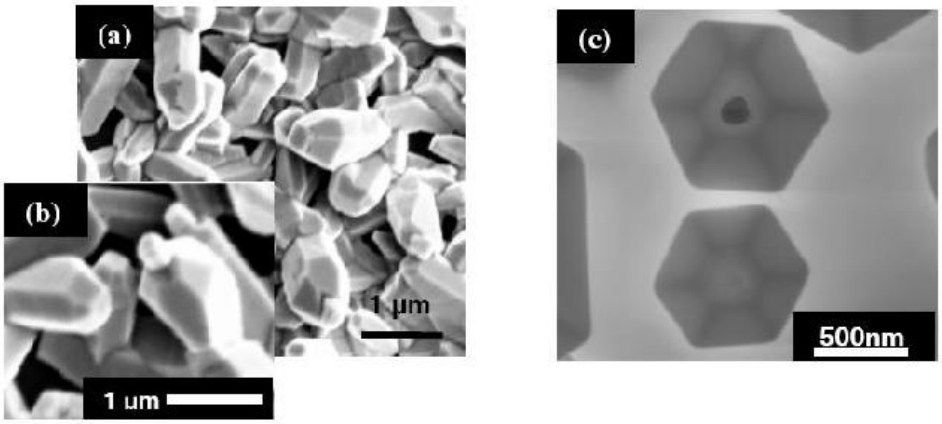

Figure 3.6: (a) SEM image of well faceted rods grown on sapphire at 525 °C with 100 sccm of Ar flow and 5 sccm of O_2 flow. (b) Magnification of as-grown rods. (c) Sample grown under the same parameters as (a) but with a shorter deposition time.

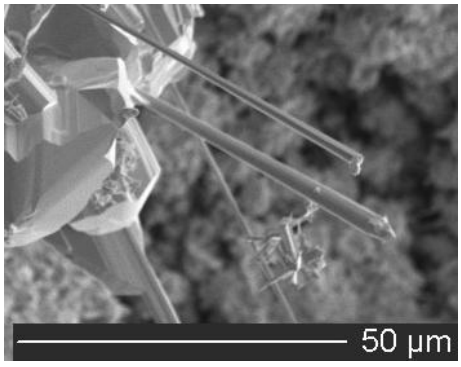

Figure 3.7: SEM image of sample growth at 650°C with 100 sccm of Ar flow and 5 sccm of O flow

3.3 Vapor Phase Transport Process (VPT)

In this process, when the vapor species are generated, the species are transported by the gas flow running through the horizontal tube furnace, and then condensed onto the surface of the substrate placed in a zone of lower temperature as shown in Fig 3.8.

The source material used in this process is Zinc acetate dihydrate, which is dried for 2h at 100 °C. After the 2 hours at 100 °C, the temperature in the furnace is elevated until it exceeds the melting point of Zn acetate (235 °C), at which point decomposition occurs.

$$\mathrm{Zn(CH_3COO)_2}(s) \rightarrow \mathrm{Zn}(v) + 2\mathrm{CH_3COO}(s^*) \tag{3.5}$$

Usually the growth temperature is set up at 500 °C [59](temperature at the center of the furnace).

When the Zn vapor is formed, it is transported by the carrier gas (a mixture of Ar and O_2) and condensed on the substrate forming liquid droplets allowing the nucleation of the crystals by oxidation as described in the previous section. From the SEM images it was found that the micro and nano-crystals were distributed uniformly on substrates placed in the zone where the temperature is in the range from 400 °C to 470 °C. Substrates placed close to the material (at 500°C) form a film and perhaps some pure acetate in addition to the ZnO. The substrates placed close to the end of the tube (at $\sim$ 350 to 300°C) present very dispersed features in the form of small clusters. Some of these results are shown in Fig.3.9.

The growth parameters for this process are summarized in Table 3.2.

Table 3.2: **Experimental parameters used in the growth of ZnO under the VTP process**

Source Material	Substrate	Temperature of material	Temperature of substrate	Deposition time	Gas Ar	Flow O_2
Zinc acetate dihydrate	Si(111) Sapphire (0001)	500 °C	from 300°C to 500 °C	2 min 3 min	from 8 to 10 sccm	5 sccm

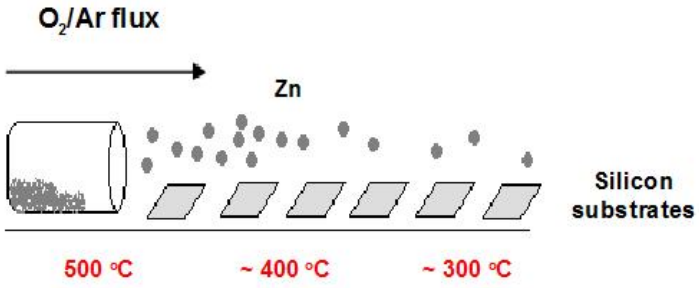

Figure 3.8: Position of the substrates and temperature gradient on the furnace

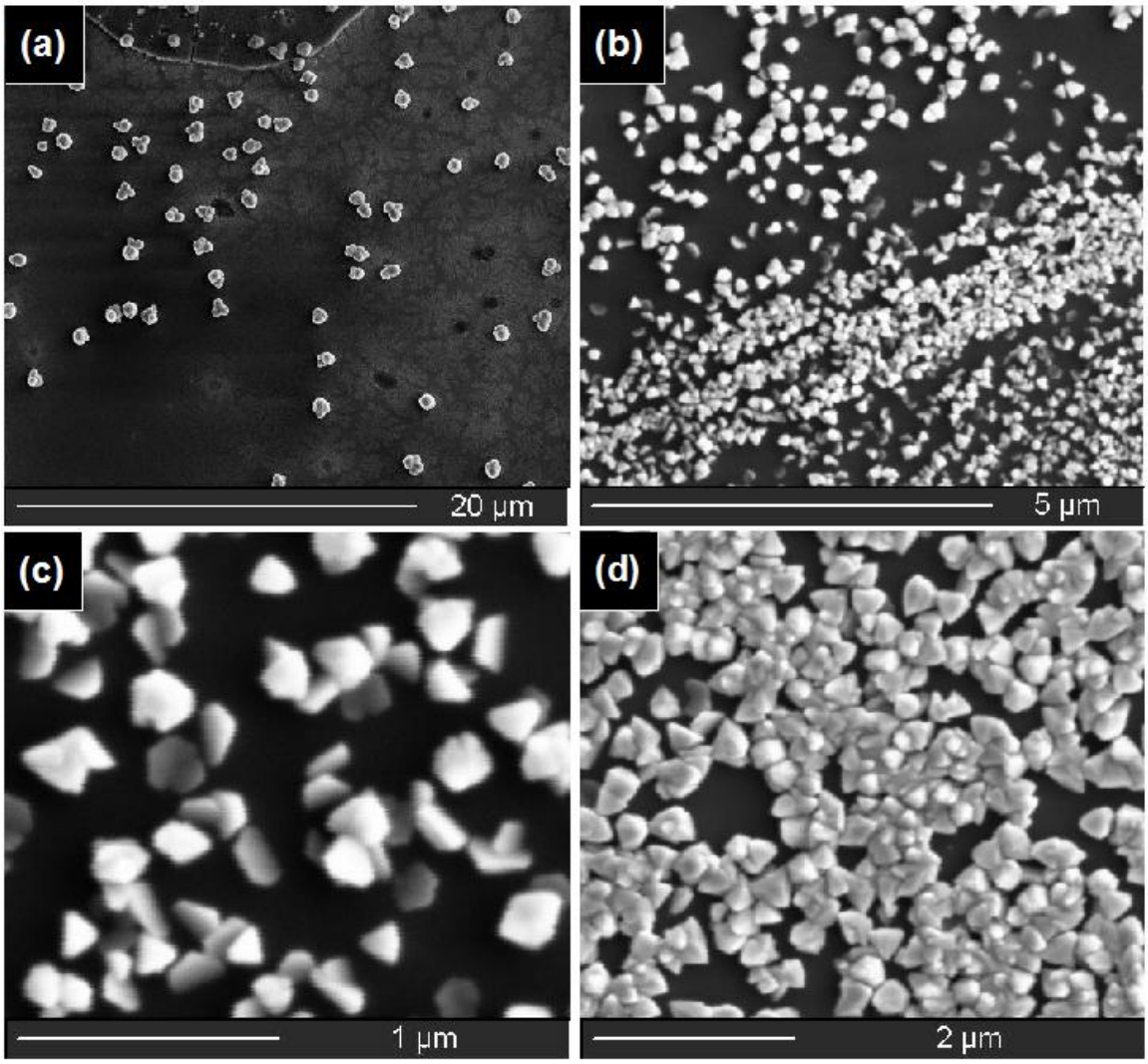

Figure 3.9: SEM images of ZnO crystals growth in substrates place at diferent positions in the furnace:(a) 350 °C (b) and (c) $\sim$ 440 °C (d) 470 °C

3.4 Nucleation and Growth Kinetics

We propose that the growth for both Vapor Phase (VP) processes can be described by the self-catalyzed vapor-liquid-solid mechanism. In the VP process, after zinc vapor species are created and condensed on the substrate, zinc micro droplets will react with O_2. The free energy change due to making a unit volume of solid is:

$$\Delta G = -V\Delta G_v + A\gamma_{SL}, \tag{3.6}$$

with V the volume of the nucleus, A the extra surface with free energy γ_{SL} per unit area created, and ΔG_v the difference in free energy between the solid and the liquid (per unit volume) [34].

For nanostructures the growth nucleus should be very small, in which case the free energy change in creating a nucleus of radius r, can be described by an approximation of the nucleus as a pill box of height l and radius r:

$$\Delta G = -\pi r^2 l\Delta G_v + 2\pi r l\gamma_{SL}. \tag{3.7}$$

Since,

$$\begin{aligned} \Delta G_v &\equiv \Delta H_v - T\Delta S_v & (3.8)\\ &= \frac{kT}{\Omega}\ln\left(\frac{P_v}{P_s}\right) & (3.9)\\ &= \frac{kT}{\Omega}\ln(1+S), & (3.10) \end{aligned}$$

with P_v the actual pressure in gas phase, P_s the saturated vapor pressure at equilibrium for a particular temperature. The supersaturation S is given by,

$$S = \frac{P_v - P_s}{P_s} \tag{3.11}$$

From equation 3.7, for small values of r, ΔG will increase with r until some critical radius r^* is reached after which ΔG decreases [34], and with it nucleation of growth centers. The critical radius and critical free energy change is calculated by differentiating Eq.3.7:

$$\frac{d(\Delta G)}{dr} = 0 \Rightarrow r^* = \frac{\gamma_{SL}}{\Delta G_v} \tag{3.12}$$

and

$$\begin{aligned} \Delta G^* &= -\pi r^{*2} l \Delta G_v + 2\pi r^* l \gamma_{SL} \\ &= \frac{\pi l \gamma_{SL}^2}{\Delta G_v} \\ &= \frac{\pi l \gamma_{SL}^2}{kTln(1+S)} \end{aligned} \tag{3.13}$$

The rate of formation of the growing nuclei is given by Brice as [34]:

$$\frac{dN}{dt} = B \exp\left(\frac{-\Delta G^*}{kT}\right) \tag{3.14}$$

with B constant, which is proportional to the number of atoms incident on the surface.

From equations 3.13 and 3.14 it is seen that crystal growth will be favored with high supersaturation (high supersaturation gives place to high nucleation rate). Ye et al. [35] have reported this relation between supersaturation and final morphology, finding that very low supersaturation favors the growth of perfect crystals with the internal symmetry; low and medium supersaturation, the growth of nanowires and nanobelts respectively; and high supersaturation, to very high supersaturation the formation of nanosheets, continuous films and poorly crystallized crystals with

undefined morphology.

In our experiments these findings were generally but not universally observed. Growing directly from the Zinc Powder, low supersaturation is achieved by controlling the temperature to the point in which Zn vapor and Zn liquid are almost in equilibrium. Then, at 500°C the smaller structures were obtained compared with larger ones grown at higher temperature. In the case of the Zinc acetate, the supersaturation is believed to be medium to high due to the decomposition process of the Zinc acetate.

In addition to the temperature, variations in the gas flow and distance from the source material were also examined to study the influence on the Zinc vapor saturation. Most of the results are consistent with the theory, however the explanation for other morphologies obtained have not been found. Fig.3.10 shows examples of various morphologies. The sample shown in Fig.3.10(a) was grown at 500 °C, 100 sccm Ar, 25 sccm O_2 which shows small thin rods. By contrast, the sample shown in Fig.3.10(b) was grown at the same temperature but 250 sccm Ar and 60 sccm O_2, shows non-uniform films.

This observation contradicts what it was reported by Ye et al. in relation to zinc vapor concentration as it varies with downstream Argon flow. It is also in contradiction with observations of our own samples *vis*. a *vis*. supersaturation. This indicates that supersaturation by itself is not a determining factor for growth morphology.

The sample in Fig.3.10(c) was grown at 650 °C, 100 sccm Argon and 5 sccm O_2. At this temperature the production of Zinc vapor is much higher, correlated with the formation of disordered structures and poor control of the final morphology of the structures even for a substrate placed at $\sim$1 cm in from the source material. This fact was also reported by Cheng et al. [36], growing ZnO nanostructures at 700 °C at an Argon flow rate of 150 sccm.

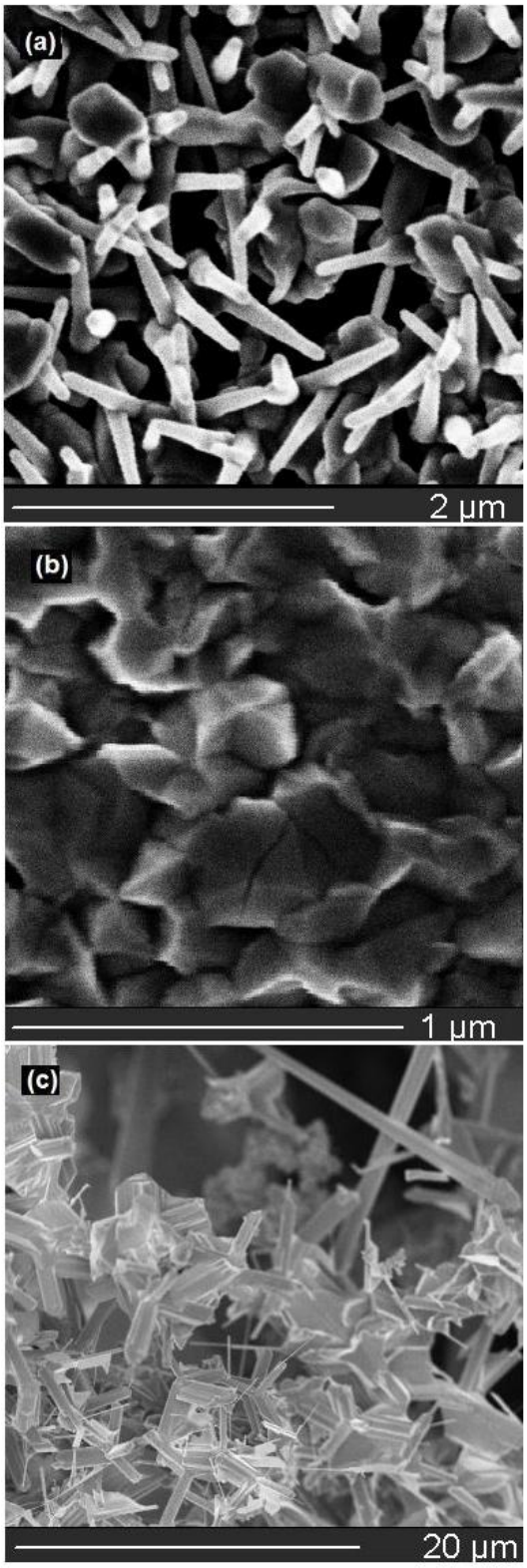

Figure 3.10: ZnO samples growth at (a) and (b) 500 °C and (c) 650 °C

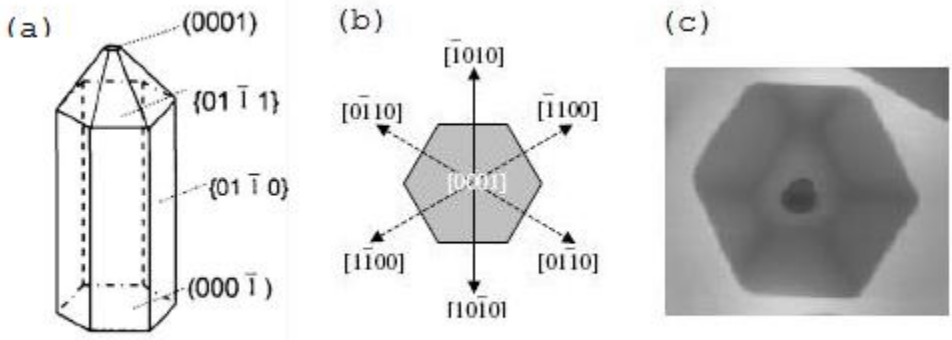

Figure 3.11: Schematic diagram showing the typical growth morphology of ZnO nanowires. Adapted from (a) Ref. [37] and (b) Ref. [2]. (c) SEM image of a sample grown in our laboratory showing the development of the facets sites in the formation of the structures

The surface energy also plays an important role since the nucleation will also be favored on those planes for which the surface free energy is the lowest. In the specific case of ZnO, the most commonly observed growth is along the [0001] direction (perpendicular to the polar surfaces $\pm(0001)$), leading the growth of the $(2\bar{1}\bar{1}0)$ or $(01\bar{1}0)$ facets, which are non-polar surfaces. The morphology of the samples prepared for the present study for which discrete nucleation could be observed, are consistent with the growth habit of the ZnO ideal crystal model [37]. This model states that the maximal crystal growth velocity is fixed in the <0001> direction and V(0001) > V$(01\bar{1}0)$ > V$(000\bar{1})$ the relationship between the velocities of crystal growth. See Fig.3.11.

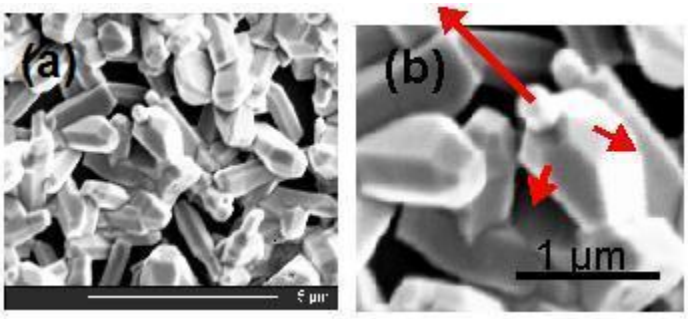

Figure 3.12: (a) SEM images of well faceted rods grown on Sapphire at 525 °C. (b) Magnification of the as-grown rods

.

Figure 3.12 present faceted rods in which both the side planes and the growth tips show well faceted planes. From this figure it is suggested that the surface energy of the polar (0001) and non-polar planes of the hexagonal structure determine the growth direction of the rods; increasing the area of the lowest surface energy planes. A magnification of the image Fig.3.12(b) shows the growth of a tip on the top of the rods. Two possible explanations for the growth of the rods are proposed. First, that the tip is driving the faster growth direction and the radial growth is slower. Second, the growth of the tip occurred at the beginning of the cooling process when Zinc vapor is reduced. This has also been reported by Wang et al [38] during the growth of ZnO nanopencils.

Chapter 4

Photoluminescence from Bulk and Nanostructured ZnO

There are many reports on optical properties and transition processes in ZnO. The next section will describe the photoluminescence study done on the ZnO micro and nano structures grown by the vapor phase technique presented in Chapter 3. It will cover the experiment setup, PL spectra obtained from the near band edge and from deep levels, and a literature review for comparison of the PL spectra obtained from our samples and the PL reported by many other research groups. A summary of some of the observed recombination processes in ZnO and the assignment to specific impurities in the material is presented as well.

4.1 Photoluminescence Setup

The Photoluminescence measurements were performed at the Wright State Semiconductor research facility at Wright-Patterson Air Force Base by collaborators.

The typical PL system includes the following parts (Fig.4.2):

1. A light source for excitation. The pump source for the PL of the as-prepared

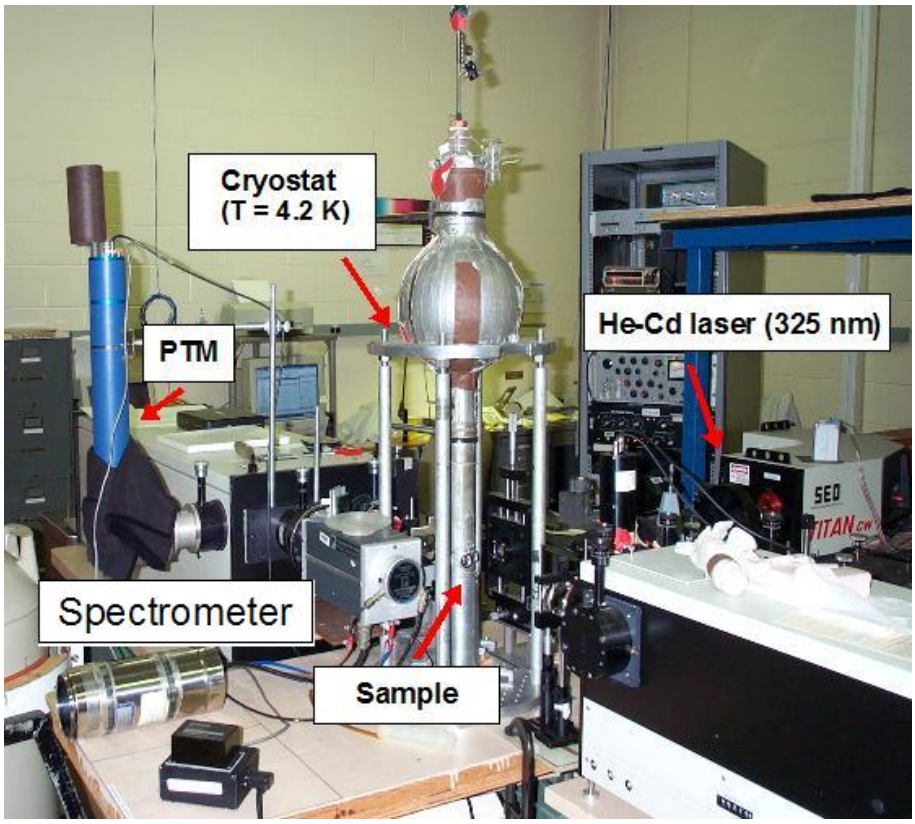

Figure 4.1: Picture of the PL system. Located at the Wright State Semiconductor research facility at Wright-Patterson AFB

ZnO samples was an Omnichrome Series Helium-Cadmium laser ($\lambda = 325$ nm) with $\sim$ 30 milliwatts output. Only a couple of milliwatts reach the sample in a focused beam of $\sim$ 100 microns in diameter.

2. An optical cryostat with a sampler holder where the temperature is 4.2 K.

3. Filters and collecting optics.

4. Spectrometer (Spex 1269) with a 1200gr/mm grating blazed at 5000 angstroms, and equipped with a C31034 photomultiplier tube with a lock-in amplifier (Princeton Applied Research Model 124A).

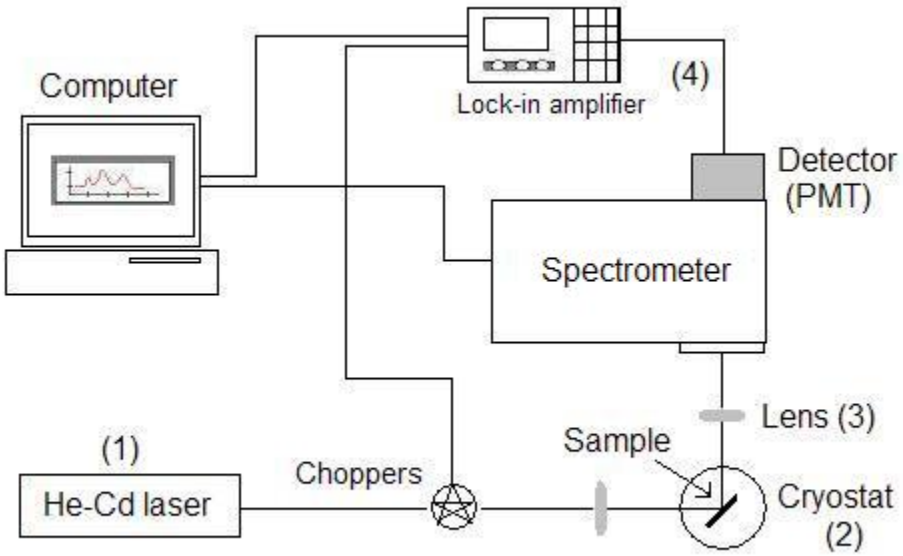

Figure 4.2: Squematic representation of the PL set-up

Measurement of photoluminescence (PL)

Before making a measurement, the intensity and position of the beam, condensing and collecting lenses and slit are all checked for optical alignment. The sample is mounted on the sample holder and the cryostat is cooled down to 4.2 K. The luminescence measurements were performed using a He-Cd laser (λ = 325 nm) as the excitation source. The emission was detected with a C31034 photomultiplier tube. The signal was chopped and the input to a Princeton Applied Research Model 124A lock-in amplifier. The PL-signal output of the lock-in amplifier was controlled and processed with Spex DM3000 software.

The spectrometer slit can be increased to enhance the PL signal from the sample and increase the signal-to-noise ratio (SNR) at the expense of spectral resolution. After the data are collected, different spectra in different wavelength range have to be normalized by slit width and photomultiplier tube gain. Finally, the PL spectra are plotted using the Easy Plot program for the further analysis.

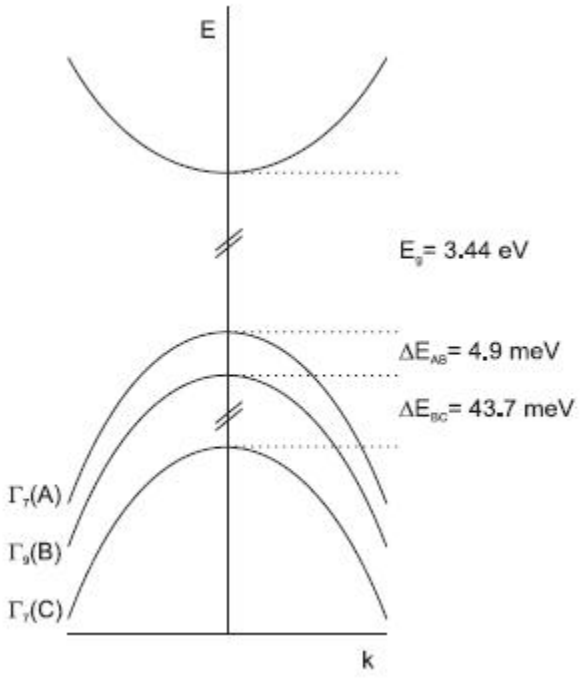

Figure 4.3: Squematic diagram representing the crystal-field and spin-orbit splitting of the valence band of ZnO into three sub-bands (A, B, C). Adapted from Ref. [12]

4.2 Optical Characteristics of ZnO

4.2.1 Free excitons

The free exciton transition involves an electron from the conduction band and a hole from the valence band. The valence band in ZnO is split by crystal field and spin orbit interaction into three bands named as A, B and C (See Fig 4.3).

There was no evidence of free excitons in the ZnO samples we examined. However, weak free-exciton transitions have been reported by many research groups. B.K.Meyer et al. report the free exciton at about 3.377 eV in bulk ZnO crystals. In a temperature dependent PL study, L.Wang and N.C.Giles [39] observed a very weak A free-exciton emission at 3.377 eV at 4.8 K, and at 3.370 eV at 100 K with an asymmetric band at 3.306 eV corresponding to the first LO phonon replica of the exciton recombination. Finally, Ozgur et al. report the "A" free exciton and excited-state transitions at

3.3771 eV and 3.4220 eV respectively at 10 K [14].

4.2.2 Bound excitons

The lines dominating the spectra of bulk ZnO originate from bound exciton recombinations, as supported by many PL studies [12, 39, 41]. Discrete exciton energy levels in ZnO are generated by the dopants (neutral or charged donors and acceptors) or defects in the material.

Table 4.1 summarizes the properties of all recombinations and assignments for the free and bound exciton recombinations at low cryogenic temperatures. The neutral donor-bound exciton (DBE) dominates normally in the low-temperature PL spectra of bulk, micro and nano-crystalline ZnO [40, 12, 41]. B. K. Meyer et al. have assigned the emission at 3.367 eV to ionized donor bound excitons [42] and the emissions between 3.3628 and 3.359 eV to neutral donor bound excitons.

The acceptor-bound excitons (ABE) are less common than the DBE. However, there have been reports of designations of the emission in the range from ∼3.35 eV to ∼3.3614 eV by Gutowski et al. [43] as ABE. The designation of the PL peaks is controversial due to the difficulty of making unambiguos designations to specific impurities or defects in the material. A typical example is a room-temperature PL analysis by Fonoberov et al. [44] for nanocrystals (NCs), quantum dots (QDs) and bulk ZnO. Their study assigned the PL emission at 3.250 eV for nanocrystals (NCs) and quantum dots (QDs) due to the recombination of bound excitons. This is awkward since the emission from the QDs is believed to be due to the recombination of the acceptor-bound excitons, at the same time the same peak from the NCs is due to recombination of the donor-bound excitons (at $T > 170$ K). Finally, for bulk ZnO the UV emission at 3.294 eV is attributed to the free excitons (Fig 4.4). These conclusions were drawn based on temperature and excitation power dependence studies (further information can be found in Ref.[44]). The acceptor-bound exciton emission from the

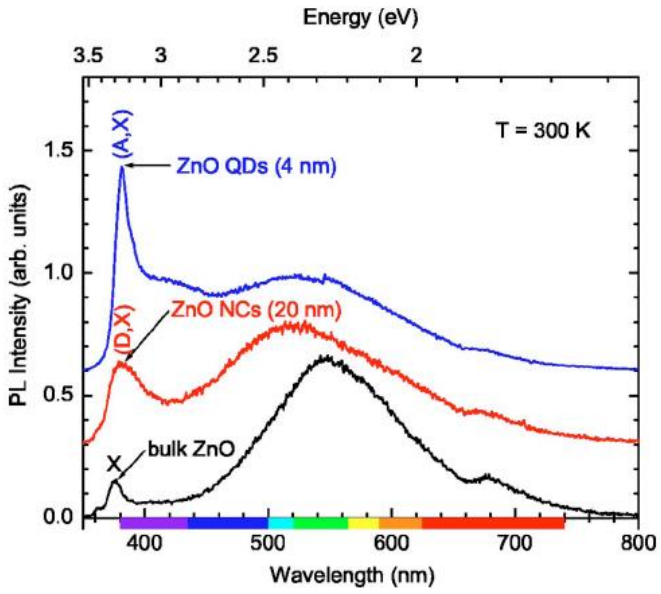

Figure 4.4: Photoluminescence spectra at RT of ZnO quantum dots, nanocrystals and bulk. From Ref. [44]

QDs was explained by the presence of surface acceptor impurities and due to the larger surface-to-volume ratio, when compared with the NCs. The presence of many surface defects affects more strongly the emission properties than the quantum confinement. Also, as is seen in Fig. 4.4, the blue shift due to the quantum confinement is not expected for the acceptor-bound excitons in the QDs because acceptors are relatively deep impurities in ZnO.

Low-temperature (4.2 K) photoluminescence spectroscopy was used to characterize the ZnO in the samples grown for the present study. The PL spectra are shown in Fig. 4.5 and 4.6. Figure 4.5 shows the PL spectra from the ZnO nanoneedles presented in Fig.1. The dominant peaks are related to a bound exciton recombination located at $\sim$ 3.359 eV, identified as Ga impurities (See line I8 in table 4.1). The emission at 3.366 eV and the shoulder near 3.35 eV have not been unambiguously identified; however, the shoulder near 3.35 eV is consistent with In-related donor-bound exciton recombination [12, 45] (line I9 in table 4.1), and the emission at 3.366

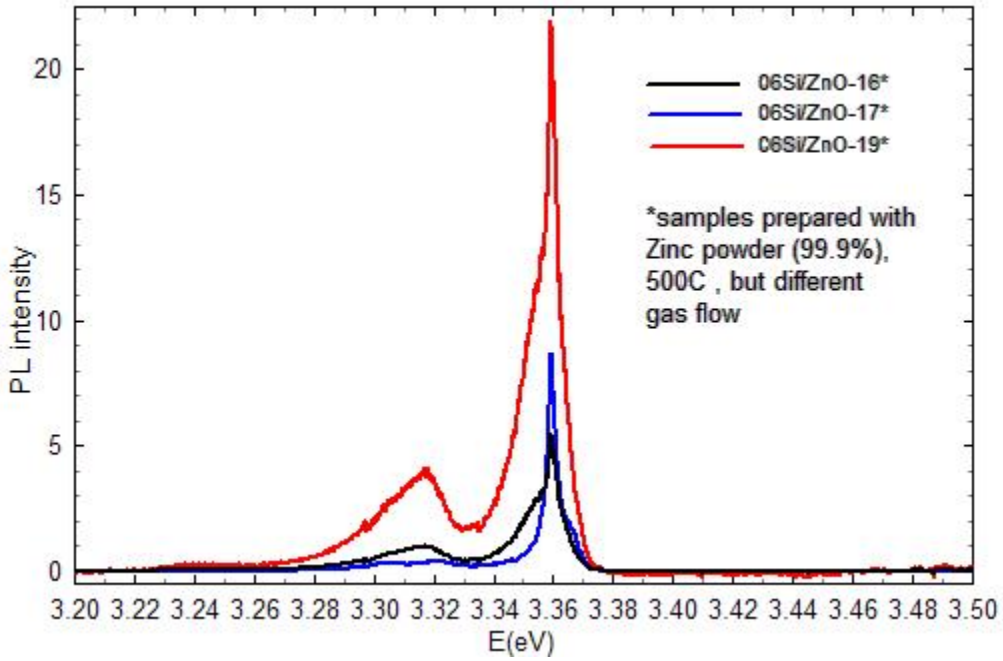

Figure 4.5: Photoluminescence spectra taken at 4.2 K from ZnO needles grown under VP process as shown in Fig.3.5

eV often occurs in the presence of known surface imperfections.

Figure 4.6 shows the UV emission from a different sample involving the faceted rods depicted in Fig. 3.12 in Chapter 3. The strongest emission from this sample, located at 3.356 eV, is normally assigned to the well known In donor-bound exciton recombination (See line I9 in table 4.1), while the second peak located at $\sim$ 3.360 eV is almost certainly related to either Ga or Al impurities [46]. The relative strength of the 3.356 eV line is somewhat surprising, since Al and Ga concentrations in ZnO are typically much higher than the In concentration. This spectral feature has also been assigned in the past to an acceptor-bound exciton [43], and Reynolds et al. [41] show that a slightly broader 3.357 eV line appears in bulk ZnO after annealing at 850 °C, and is definitely not related to In. Thus, an exciton bound to In is not the only possibility for this line and the true assignment must await further investigation.

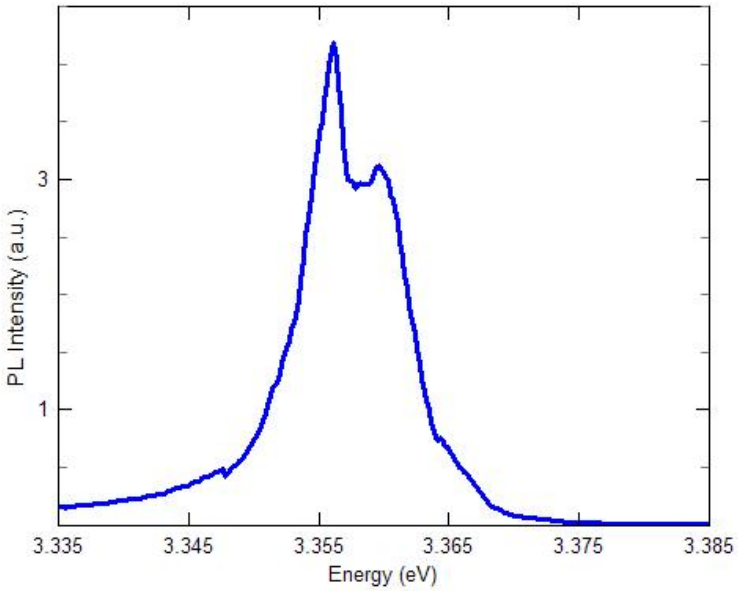

Figure 4.6: Photoluminescence spectra taken at 4.2 K from faceted ZnO rods as shown in Fig.3.6

Table 4.1: **Free and exciton recombinations and related properties.** *Adapted from: B. K. Meyer, H. Alves, D. M. Hofmann et. al., Phys. Stat. Sol.(b),* **241, 231 (2004)**

Line	Wavelength (nm)	Energy (eV)	Localisation energy (meV)	TES separation $(2P_{xy} - 1S)$(meV)	Donor binding energy (meV)	Chemical identity
A_L^*	367.12	3.3772				
A_T^*	367.26	3.3759				
I_0	367.63	3.3725	3.4			
I_1	367.71	3.3718	4.1			
I_{1a}	368.13	3.3679	8.0			
I_2^{**}	368.19	3.3674	8.5			
I_3^{**}	367.63	3.3725	9.4			
I_{3a}	368.34	3.3660	9.9			
I_4	368.34	3.3628	13.1	34.1	46.1	H
I_5	368.86	3.3614	14.5			
I_6	368.92	3.3608	15.1	38.8	51.55	Al
I_{6a}	368.96	3.3604	15.5	40.4	53	
I_7	369.01	3.3600	15.9			
I_8	369.03	3.3598	16.1	42.1	54.6	Ga
I_{8a}	369.08	3.3593	16.6			
I_9	369.37	3.3567	19.2	50.6	63.2	In
I_{10}	369.76	3.3531	22.8	60.2	72.6	
I_{11}	370.28	3.3484	27.5			

4.2.3 Donor acceptor pairs

Figure 4.7 shows a comparison of the PL spectra for nano/micro-structures grown under different temperatures (500 °C (13) and 650 °C (31)), different gas flow rates and materials (zinc acetate and zinc powder). Emission at the near-band edge (NBE) are due to either impurities or surface defects. The peaks at lower energies, 3.294 eV and 3.308 eV are related to donor-acceptor pair transitions by quantitative analysis of the peaks. The energy of a donor acceptor pair can be calculated as,

$$E_{\mathrm{DAP}} = E_g - E_D^{\mathrm{bind}} - E_A^{\mathrm{bind}} + \frac{e^2}{4\pi\epsilon_0\epsilon R_{\mathrm{DA}}} \tag{4.1}$$

where E_g is the band gap (3.437 eV at 4.2 K [44]), E_D^{bind} is the binding energy of a donor, E_A^{bind} the binding energy of an acceptor, ϵ_0 the permittivity of free space, e the electron charge and ϵ the dielectric constant for ZnO ($\epsilon = 8.2$ [47]), and R_{DA} is the donor-acceptor separation.

The donor-acceptor separation R_{DA} is calculated using the following approximation with a donor concentration N_D of the order of $10^{18}\mathrm{cm}^{-3}$:

$$< R_{\mathrm{DA}} >= (\frac{3}{4\pi N_D})^{\frac{1}{3}} \tag{4.2}$$

$$= 6.204 \text{ nm} \tag{4.3}$$

and the Coulombic term,

$$\frac{e^2}{4\pi\epsilon_0\epsilon R_{DA}} = \frac{1.44eVnm}{\epsilon R_{DA}} = 28.3 \text{ meV} \tag{4.4}$$

Using the result of equation 4.4, it is possible to evaluate wheter the peaks at 3.294 eV and 3.308 eV are donor-acceptor pairs. From Eq.(4.1) and using the values

of each of the peaks, we find the suspected-acceptor binding energy to be:

$$3294 \text{ meV} = 3437 \text{ meV} - 55 \text{ meV} - E_A^{\text{bind}} + 28.3 \text{ meV}$$
$$E_A^{\text{bind}} = 116 \text{ meV} \tag{4.5}$$

$$3308 \text{ meV} = 3437 \text{ meV} - 55 \text{ meV} - E_A^{\text{bind}} + 28.3 \text{ meV}$$
$$E_A^{bind} = 102.3 \text{ meV} \tag{4.6}$$

The estimated values 116 meV and 102.3 meV are in good agreement with both the hydrogenic model (Eq.4.7) and the reported values for the acceptor binding energy for ZnO [44, 17].

$$\frac{13.6 m_h^*}{m_0 \epsilon_0^2} = 119.33 \text{ meV}, \tag{4.7}$$

with m_h^* the hole effective mass of $0.59 m_0$ [47]. The value of the donor-acceptor transition energy will vary with the impurities (donors and acceptors) involved in the transition. However, there was insufficient evidence to identify the impurities associated with these donor-acceptor pair transitions.

The DAP luminescence centered at 3.323 eV has also been observed by Xiong et al. [48] in nitrogen-doped samples for which the calculated acceptor binding energy is 177 meV. Thonke et al. [49] has also observed a DAP transition at 3.232 eV, believed that the acceptor participating in the transition is N substituting on an oxygen site.

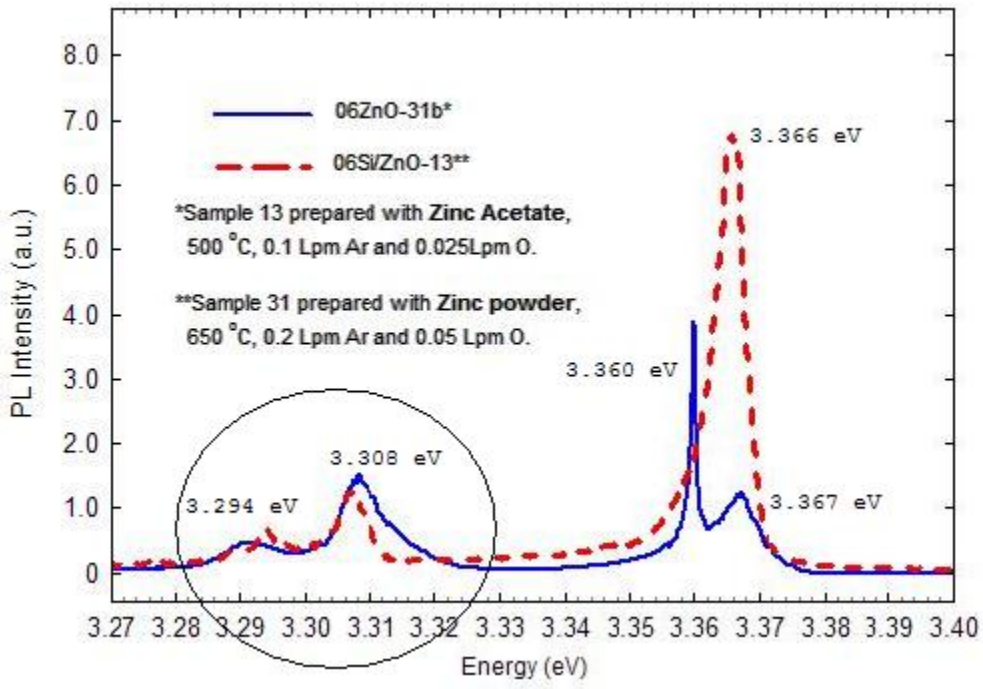

Figure 4.7: Photoluminescence spectrum of two samples prepared at 500 °C (sample 06Zn0-13) and 650 °C (sample 06ZnO-31)

4.2.4 Two electron satellite (TES)

The two electron satellite (TES) transition occurs if in the bound exciton recombination process the neutral donor is excited from its ground state (1s) to an excited state (2p,3p,...). In the hydrogenic effective-mass-approach, the energetic distance between the neutral donor and its TES is the difference between the donor energies in the 1s and 2p states, which is 3/4 of the donor binding energy.

Using this approach and by determining the position of the TES recombination lines (lines expected to be located in the region from 3.31 to 3.34 eV as a mirror of the principal bound exciton spectrum), Thonke et al. [49] have determined the donor binding energy of the donor-bound exciton related to the lines I4 and I8 (see table 4.1). These lines were replicated at 29.9 meV lower energy, having an ionization energy of 4/3 x 29.9 meV = 39.9 meV . Meyer et al.[12] also reported the presence of TES recombination lines coresponding to the bound excitons designated as I4, I6, I8 (See table 4.1) in undoped ZnO. From the location of the TES lines (Fig. 4.8) the related donor binding energy was calculated with good accuracy corresponding to the values of 51.55 meV for I6, 53 meV for I6a and 54.6 meV for I8 donor lines (for details in calculation see Ref [12]).

The TES transitions were not observed in the PL spectra taken in the ZnO samples prepared for this work.

4.2.5 Deep impurities

Another common optical feature of ZnO is a broad defect related peak extending from $\sim$ 1.9 to $\sim$ 2.8 eV, known as the green band. The origin is still not well understood and it has in the past been attributed to a variety of different impurities and defects.

Figure 4.9 shows the green band emission centered at $\sim$ 2.45 eV obtained from two of the as-grown samples under different Argon flow rates. The plot shows the higher intensity for the sample grown under higher Ar flow (06ZnO-19) suggesting that the

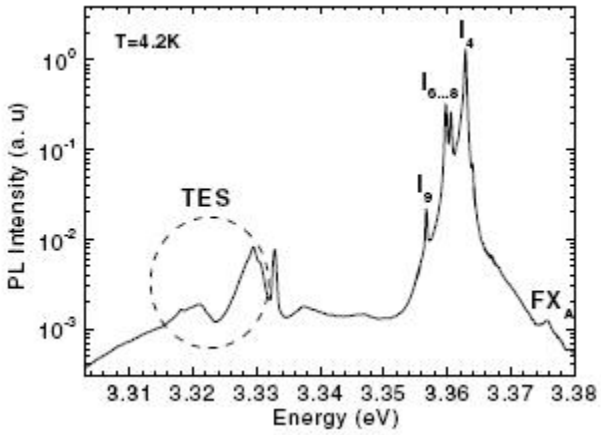

Figure 4.8: Photoluminescence from bulk ZnO showing the bound exciton lines I4 to I9 and their corresponding two electron satellite emission. From Ref.[12]

origin of the green band emission in this sample may be oxygen vacancies due to the deficient amount of oxygen during the growth. The assignment of the green emission due to the oxygen vacancies corresponds with other works. For example, Cheng et al [36] have reported the enhancement of the green-band emission due to oxygen vacancy formation. In that study the different concentrations of oxygen vacancies were created during growth at different argon flow rates, thus, the higher the argon flow rate, the lower the oxygen content and with it the formation of more oxygen vacancies. Also, Zhang et al. have proposed electron-hole radiative recombination at the oxygen vacancy center as the source of the green luminescence [50].

However, in the PL spectra shown in Fig 4.9, the near-band edge (NBE) intensity from sample 19 is significantly higher than that from sample 16; so much so that the ratio of the green-band PL to the NBE PL is actually lower in sample 19 than it is in sample 16. If the difference in NBE PL intensities between the two samples is simply due to a higher concentration of non-radiative centers in sample 16, then the lower green-band intensity in sample 16 may result from the same reason, rather than from a lower concentration of green-band centers. Thus, our results do not necessarily support the O-vacancy assignment for the green band.

The green band emission has also been assigned to the luminescense transitions at divalent copper impurities by R. Dingle [51] and N. C. Giles et al [52] using photoluminescence and electron paramagnetic resonance (EPR).

In order to make a comparison between the green band (deep) and NBE PL spectra, it is necessary to normalize the data due to the adjusments made in the slits and gain voltage in the detection system when taking each part of the spectra. For the specific case of the PL spectra presented in Fig.4.9, the data were normalized to a gain of 5 mV and slits of 144 μm. The procedure is as follows:

	NBE		Deep	
Sample	Gain (mV)	Slit (μm)	Gain (mV)	Slit (μm)
16	5	32	10	144
19	20	32	10	144

From the numbers on the table: a full-scale signal on the 10 mV scale has twice as much absolute intensity as a full-scale signal on the 5 mV scale. On the other hand, a full-scale signal requiring slits of 144 μm has only $(\frac{32}{144})^2 = \frac{1}{20.25}$ of the strength of a full-scale signal with slits of 32 μm. This procedure was also applied to all the other PL spectra reported in this work.

Figure 4.10 presents the PL deep spectra from the grown ZnO faceted rods presented in Fig.3.4. The red-orange emission (peak at $\sim$1.5 - 1.9 eV) has not been as commonly observed as the green and yellow emissions. The origin of this emission is also controversial. The yellow/orange emission is associated with oxygen interstitials [53] while the green emission is typically associated with oxygen vacancies. Djurišić et al. [54] studied the luminescence in the visible spectral range (green, yellow, and orange emissions), and indicated that there is a dependence of this emission on the excitation wavelength and fabrication conditions.

The assignment of red/orange luminescence to oxygen interstitials or the dependence on excitation wavelength is not supported by the spectrum shown in Fig.4.10.

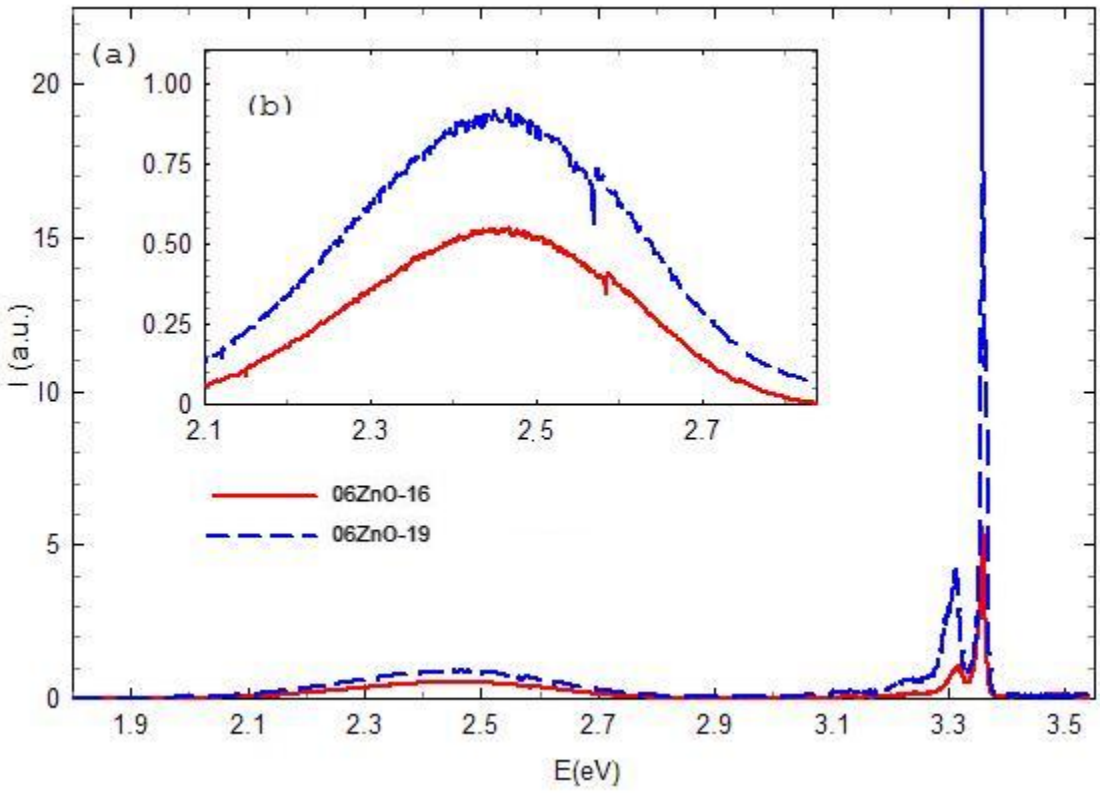

Figure 4.9: (a)Photoluminescence of the near band edge and green band emission of the samples 16 and 19 presented also in Fig (4.5). (b)Expanded view of the green band emission

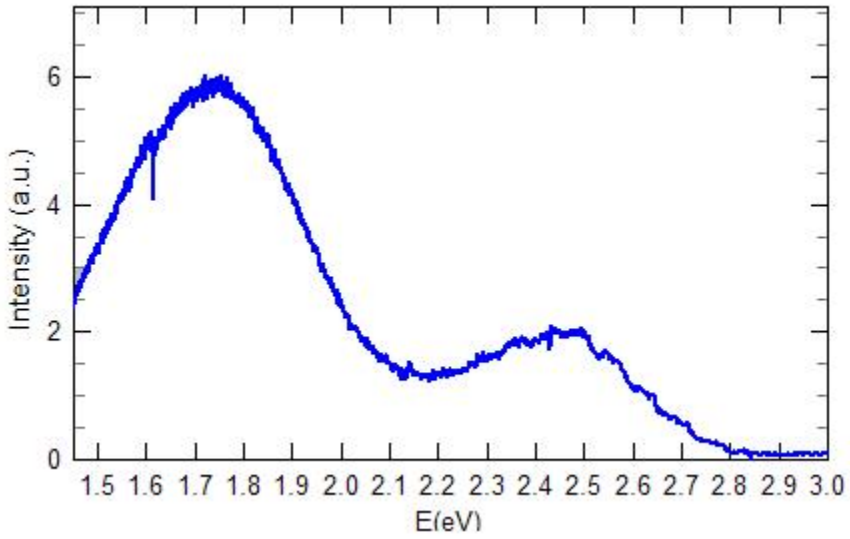

Figure 4.10: (a)Photoluminescence of the deep band emission corresponding to the near band PL show in Fig 4.6

Referring to table 3.1 and comparing the experimental growth parameters, the sample corresponding to the present spectra has the lowest concentration of oxygen (5 sccm) contradicting the involvement of the oxygen interstitials. On the other hand, all of the PL spectra in this work have been taken under the same excitation wavelength and no other PL spectra from other samples show red emission. Then, no conclusions about the origin of the observed features can be drawn.

Defects in ZnO

Photoluminescence at low temperature together with theoretical calculations [55] is widely used to investigate point defects in ZnO. Determination of the relevant native defects of ZnO have been a topic of controversy among experimental and theoretical studies.

The formation energies and electronic structure of native point defects in ZnO were calculated by Van de Walle et al. [55] using ab initio, first principles pseudopotential method (pseudopotential calculations are describe in Ref.[56]). The results

are presented in the Table 4.2, which shows all the native-points formation energies E_f in ZnO.

The formation energies of all the native point defects in ZnO were computed using the following formalism. The relatioship between the concentration of defects in a crystal and their formation energy is determined by,

$$c = N_{\text{sites}} \exp(-\frac{G^f}{k_B T}), \tag{4.8}$$

where N_{sites} is the concentration of available sites in the crystal where the defect can occur (per unit volume), T the temperature and k_B the Boltzmann constant. The free energy of formation G^f is given by,

$$\Delta G_f = \Delta E_f - T\Delta S_f + P\Delta V_f \tag{4.9}$$

In this case, the biggest contribution comes from the change of the total energy of the system ΔE_f or formation energy. The dependence of G_f with PΔV is negleted since the change of volume is relatively small when the defect is introduced, and the term ΔS (vibrational entropy) is also neglected due to the similarity of the structures compared, so that the change of entropy is small at normal temperatures [57]. However, at high temperature, strong rearrangements occur in the lattice of the crystal, making neccesary the consideration of the term $T\Delta S$. In the study done by Van de Walle et al. [55] the system is treated for constant volume and entropy conditions.

The formation energy of a charged point defect in ZnO is given by,

$$\Delta E_f = E^{tot}(N_{Zn}, N_O) - N_{Zn}\mu_{Zn} - N_O\mu_O + q\epsilon_F \tag{4.10}$$

where E(N_{Zn}, N_O) is the total energy of the system, N_{Zn} and N_O zinc and oxygen atoms, μ_{Zn} and μ_O the zinc and oxygen chemical potentials, q is the number of electrons or holes including the sign of the charged defects and ϵ_F the Fermi level,

which is taken as the energy of the reservoir (chemical potantial) from which an electron is removed (or placed) to form a charged defect [55].

The defect formation energies were studied within the range of oxygen and zinc chemical potentials in which ZnO can exist which are given by:

$$\mu^0_{Zn} + \Delta E_f^{ZnO} < \mu_{Zn}^{ZnO} < \mu^0_{Zn} \tag{4.11}$$

using the formation energy of ZnO from metallic Zn and O_2 gas:

$$\Delta E_f^{ZnO} = \mu_{Zn}^{ZnO} - \mu^0_{Zn} + \mu_O^{ZnO} - \mu^0_O, \tag{4.12}$$

with μ_{Zn}^{ZnO} the chemical potential of Zn in ZnO, μ^0_{Zn} energy of Zn in the stardard state (pure metal) ($\mu_{Zn}^{ZnO} < \mu^0_{Zn}$, to prevent pure Zn formation, μ_O^{ZnO} the chemical potential of O in ZnO, μ^0_O energy of pure O_2 gas (per oxygen atom) ($\mu_O^{ZnO} < \mu^0_O$, to prevent oxygen loss). Also, the Fermi energies correspond to heavily doped p-type ($\epsilon_F = 0$) and heavily n-type ($\epsilon_F = 3.4eV$) ZnO.

Finally, based in the data in Table 4.2 it is concluded that the dominant native defects in ZnO are zinc and oxygen vacancies. The neutral oxygen vacancies have an energy of 0.02 eV and the neutral zinc vacancies have an energy of 1.46 eV. Both energies are the lowest positive formation energy for charge complementary defects under both heavily doped n and p type conditions. Other defects that are listed with low, or negative, formation energies in Table 4.2 are representative of the chemical forcing of defect formation under the extreme conditions of heavy doping. The calculations indicate that the least energetically favorable defects are the zinc and oxygen antisite defects.

Table 4.2: **Formation energies of native-point defects in ZnO.** *Adapted from: A. F. Kohan, G. Ceder, D. Morgan, and C. G. Van de Walle Phys.Rev.B* **61, 15 019(2001)**

Defect	Charge on defect	$E_f(\mu_{Zn} = \mu^0_{Zn})$ $\epsilon_F = 0eV$	[eV] $\epsilon_F = 3.4eV$	$E_f(\mu_{Zn} = \mu^0_{Zn} + \Delta_f^{ZnO})$ $\epsilon_F = 0eV$	[eV] $\epsilon_F = 3.4eV$
Zn_i(oct)	0	1.73	1.73	5.74	5.74
Zn_i(oct)	+1	1.28	4.68	5.29	8.69
Zn_i(oct)	+2	0.87	7.67	4.88	11.68
Zn_i(tet)	0	2.92	2.92	6.93	6.93
Zn_i(tet)	+1	2.61	6.01	6.62	10.02
Zn_i(tet)	+2	2.40	9.20	6.41	13.20
O_i(oct)	-2	7.76	0.96	3.75	-3.046
O_i(oct)	-1	6.81	3.41	2.80	-0.59
O_i(oct)	0	6.43	6.43	2.42	2.42
O_i(oct)	+1	6.40	9.80	2.39	5.79
O_i(tet)	-1	7.49	4.09	3.48	0.08
O_i(tet)	0	6.50	6.50	2.49	2.49
O_i(tet)	+1	6.50	9.90	2.49	5.89
V_{Zn}	-2	6.60	-0.20	2.59	-4.21
V_{Zn}	-1	5.82	2.42	1.80	-1.59
V_{Zn}	0	5.47	5.47	1.46	1.46
V_O	0	0.02	0.02	4.02	4.02
V_O	+1	0.15	3.55	4.16	7.56
V_O	+2	-0.32	6.47	3.69	10.49
Zn_O	0	2.41	2.41	10.43	10.43
Zn_O	+2	0.55	7.35	8.56	15.63
O_{Zn}	-2	11.98	5.18	3.97	-2.83
O_{Zn}	0	9.74	9.74	1.72	1.72

Chapter 5

Capacitance-Voltage (C-V) profiling in bulk ZnO

Measurement of the capacitance, carrier concentration and depth profiling of ZnO can be performed using the electrochemical capacitance-voltage (ECV) profiling technique. It is based on the measurement of the capacitance of an electrolyte-semiconductor Schottky contact at a constant dc bias voltage combined with an optional electrolytical etching of the semiconductor between measurements.

This technique can provide information about the 'doping profile' in the semiconductor. One of the advantages is that, although the method is destructive, the profile can, in principle, be measured to unlimited depth [31, 32].

However, so far, there are not many reports on the characterization of ZnO by electrochemical C-V profiling. C. E. Stutz [64] has reported depletion capacitance-voltage (CV) measurements on bulk ZnO, but no successful depth profiling (etching) of the material using 0.2M NaOH/0.1M EDTA. X. Tang et al. [60] reported results of the C-V profiles obtained from ZnO thin films and showed that the electrochemical profiling of the ZnO layers can be obtained routinely and reproducibly by using 0.1M $ZnCl_2$ as the electrolyte solution.

This section will present the results and some conclusions found in the characterization of ZnO using the ECV profiling technique. The characterization was made on different ZnO samples (bulk, thin films, micro- and nano-structures) and with two different electrolytes, 0.1 M Tiron and 0.1M $ZnCl_2$. Unfortunately it was not possible to profile the ZnO micro and nanostructures for reasons discussed below.

5.1 Electrochemical C-V Profiling Setup

The ECV profiling in ZnO is performed in an electrochemical cell shown in Fig. 5.1. The functions of the cell are: 1) to hold the sample by means of spring-loaded back contacts against the sealing ring that defines the electrolyte contact area; 2) to provide the ohmic contact to the sample by means of probe wires; 3) to house the electrodes and electrolyte and to provide an electrical interface to the rest of system; 4) to allow uniform illumination of the semiconductor/electrolyte interface for etching purposes.

The electrolyte is used to make a Schottky barrier and, if etching, to remove controlled amounts of material per unit charge passed during the etching. A front or back contact system is used to make ohmic contacts to the sample.

Both etching and CV measuring conditions are controlled by the DC potential across the cell. This is established by passing a DC current between the semiconductor and the electrolyte's counter electrode to maintain the required contact potential measured with respect to the saturated calomel electrode (Fig. 5.1). To reduce series resistance due to the electrolyte, the ac voltages are measured with a platinum electrode (Pt) located near the sample. In response to the ac voltage the charges that move are the mobile holes (in p-type material) or mobile electrons (n-type material). The carrier density measurement is based on Eq.2.10.

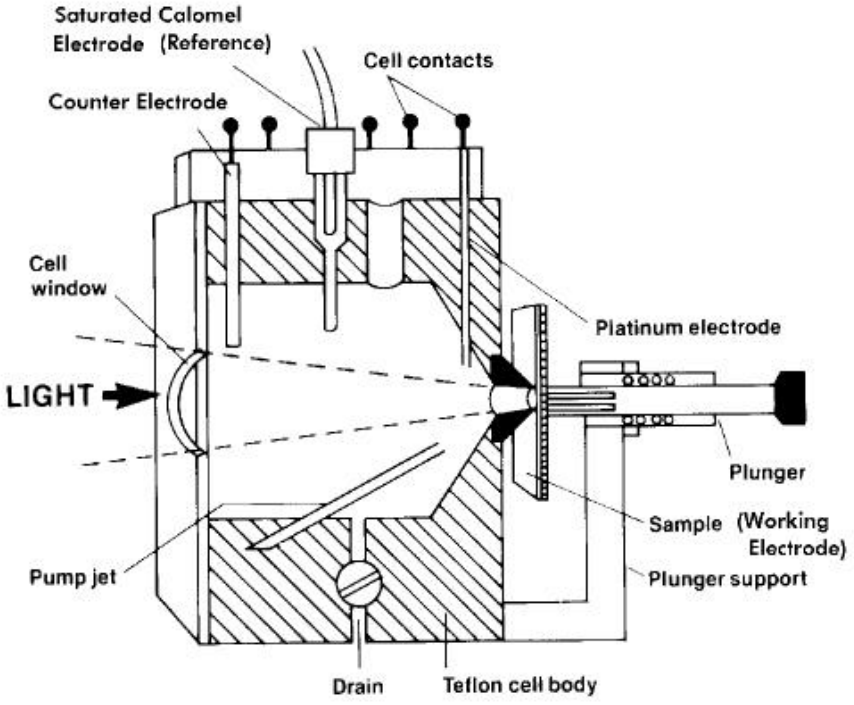

Figure 5.1: Diagram of the electrochemical cell used for the ECV profiling measurements. Adapted from Ref.[65]

5.2 ECV Profiling Measurement

For this study, the measurements were performed using a Accent PN4200 photoelectrochemical system, and associated PN4300 software. The sealing ring size used is the large ring (Area = 0.1 cm^2, 3.5 mm diameter). This choice is made depending on the sample size, but principally on the carrier concentration levels encountered when profiling the sample. The front contact configuration was used to make the ohmic contact to the sample's surface.

The selection of the electrolyte is key to the correct functioning of the system. It forms the electrical contact with the semiconductor, similar to a Schottky diode; and, under the correct conditions, it will etch the semiconductor by an electrochemical dissolution reaction with the semiconductor when a charge is passed through the interface. For the profiling of ZnO two separate electrolytes were used, 0.1M $ZnCl_2$ and Tiron [60, 64].

The properties of the material to be etched and the electrolyte are saved in the software before making any measurement. These data are needed for calculation by the software of the etched depth (Eq.2.11), depletion depths (Eq.2.8) and finally carrier concentration (Eq.2.10).

The ZnO bulk samples characterized in this work were grown by Cermet, Inc. [66], using a pressurized melt-growth technique [67].

There are four stages in obtaining an ECV profile:

1. **Obtain an I/V plot from which it is possible to derive the appropriate bias voltage range for the capacitance measurement**.

   One of the purposes is to check the quality of the ohmic contacts looking for the abruptness in the forward bias breakdown. The lower left quadrant of the IV curve shown in Fig. 5.3 shows the breakdown forward bias breakdown for a typical n-type material (Note: the presentation of the IV curve in this system

is backwards from the normal metal-semiconductor IV plots). The forward breakdown should be seen in the IV plots for both dark and illuminated samples.

The second purpose of the IV curve is to determine the voltage range over which the contact potential is not dominant and the limits of the sample's diode region. The usable diode region is selected from an IV curve taken under illuminated conditions as described below.

The illuminated IV will indicate the conditions required for etch profiling later. Since for n-type material the etching takes place under illuminated, reverse bias conditions to generate a hole current, the etch voltage (V_{etch}) should be selected in the flat (voltage independent) region of the IV curve (vertical red line in Fig. 5.3).

2. **Using the bias voltage range derived from the I/V plot a C/V plot is obtained, and this is used to derive the measurement potential required to create etching conditions**.

   In the acquisition of the CV plot, the quality of the electrochemical diode is evaluated. The CV plot presented in Fig. 5.2 is a good example of a Schottky model contact. The results for the series (green line) and parallel (blue line) resistance models used to analyze the diode response are coincident over the majority of the reverse bias voltage range. The dissipation factor (D-factor)(red line) also remains very low (below the 0.4 level).

   The small horizontal red line indicates the DC bias voltage (V_{meas}) that is used during electrochemical carrier concentration profiling. The width of the cursor indicates the amplitude of the AC signal. This cursor is placed in the region where the D-factor curve is below 0.4 , and where the $1/C^2$ plot is a straight line (See Fig. 5.2).

3. **Measurement of the depletion profile**.

   A concentration profile can be obtained without etching the sample by using the depletion profile. This plot is useful to obtain data near the surface and to determine the correct V_{meas} for the electrochemical etch profiling. The concentration can be plotted as a function of voltage, depletion depth, or total depth. Plotting log concentration vs voltage will allow the determination of the correct V_{meas}. Most of the time this will be the point at which the carrier concentration in the depletion profile approaches a constant value. See Fig. 5.4.

4. **Using all the information obtained above, perform the etch profile**.

   Once the electrochemical Schottky diode is formed and the electrical characteristics are investigated to determine the conditions for an etch of the sample, the profile of carrier concentration versus depth can be obtained Fig. 5.5. The etch profile is obtained from the concentration taken from a series of depletion profiles as described in step three above-one after each etch. The dark blue bar indicates the etched depth (W_r) and the light blue bar indicates the depletion width (W_d). The total depth is given by the sum of the etch depth and the depletion depth.

5.3 Carrier Concentration in Bulk ZnO

From the CV curve Fig. 5.2 the V_{meas} parameter set was $\sim$0.3 V. From the IV curve Fig. 5.3 it was set the V_{etch} of about 0.13 V and it was increased during the etching. This voltage should keep the etching current (I_{etch}) less than 0.1 mA/cm^2 (as determine for the system). From the depletion profile plot in Fig. 5.4 and the slope of $1/C^2$ presented in the CV plot in Fig. 5.2, the sample was shown to have a doping level near the surface of about 4×10^{17}cm^{-3} and is n-type (Note that this profile is taken without etching). To get concentrations deeper into the sample an etch profile

was also taken, see Fig. 5.5. The etch profiling of the sample shows a very uniform concentration up to a depth of ~ 0.3 μm. The concentration is $\sim 3.85 \times 10^{17}\text{cm}^{-3}$. The sample used had previously been examined by Hall measurements presenting a concentration of $8.6 \times 10^{16}\text{cm}^{-3}$.

From the results above it is concluded that the system works very well for bulk samples, in which the ohmic and Schottky contact are well formed using 0.1M $ZnCl_2$ as the electrolytic solution. However, the profiling could not be performed using thin films. Using a ZnO thin film sample (B8) with a thickness of 0.1009 μm over a glass substrate, and samples prepared in our laboratory believed to be nominally continuous, a good ohmic contact could not be formed. Thus, neither depletion nor depth profiling could proceed. The instrument manual suggests that some of the reasons for poor contact formation are:

- Low-doped layers on semi-insulating or opposite carrier type substrates.
- Low-doped bulk samples
- Low-doped or thin layers on conducting substrates with insulating oxide on the back surface.
- Thin (<0.25 mm) layers grown on semi-insulating substrates.

The B8 sample was grown on an insulating substrate (glass) and it is a very thin layer. Our samples were grown on Si substrates, which is much likely to have an oxide layer. These factors affect the formation of a good ohmic contact with low resistance (ideally in the range from 50 to 200 Ω), therefore, other techniques must be employed before the measurement can be undertaken. A GaIn eutetic (liquid at room temperature) can be painted on the surface of an oxide-free surface to form an ohmic contact between the semiconductor and the contact pins. Other possibilities are the use of silver paint or evaporated contacts. Ga-In was used in our samples, however, the

eutectic could not be made to adhere to the sample. Additional research is necessary for effective contact formation to thin films or quasi-continuous depositions, in order to have successful profiling of these types of samples.

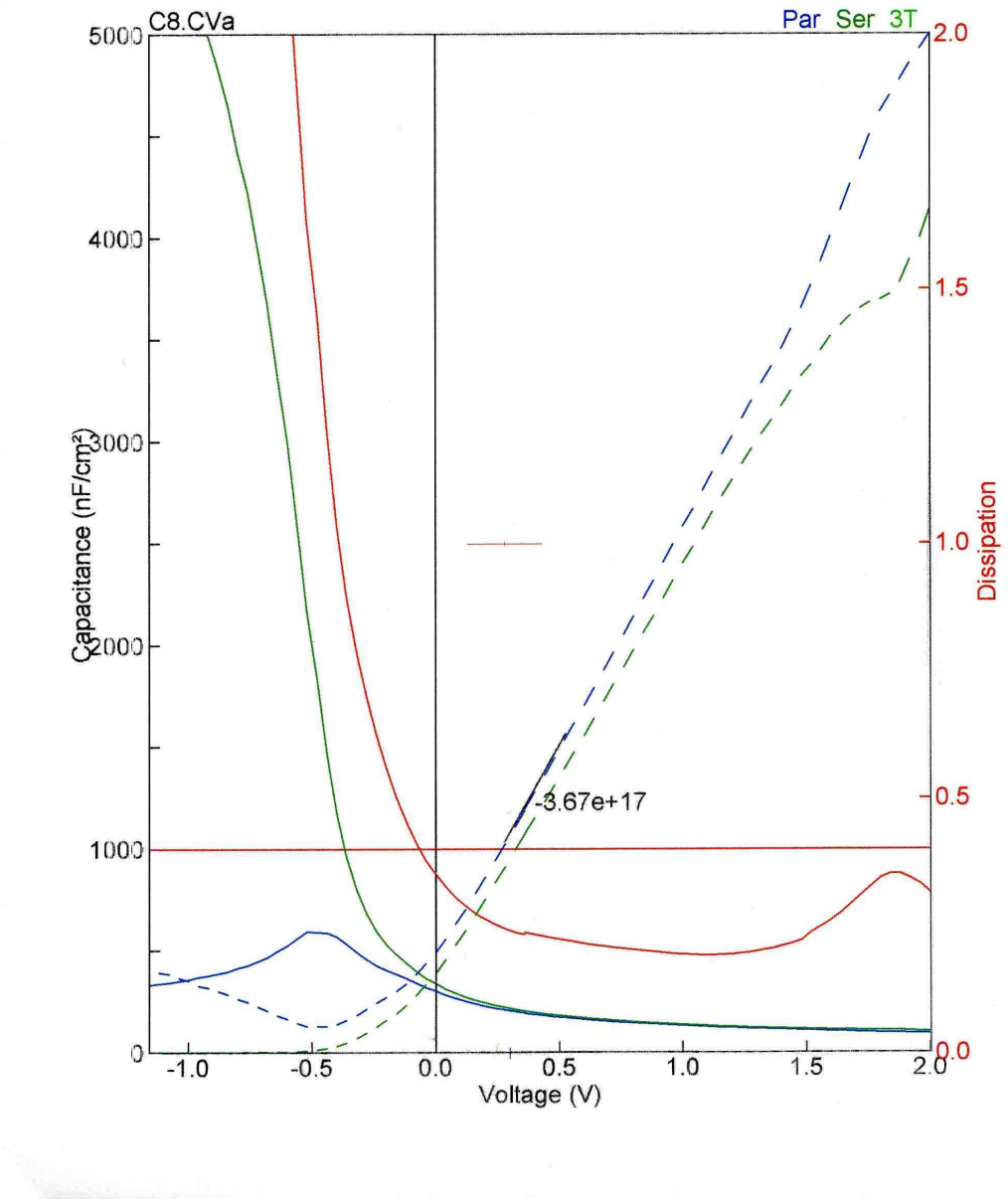

Figure 5.2: Capacitance versus voltage, together with $1/C^2$ curves for n-type bulk ZnO using 0.1M $ZnCl_2$ as the electrolyte to form the Schottky contact

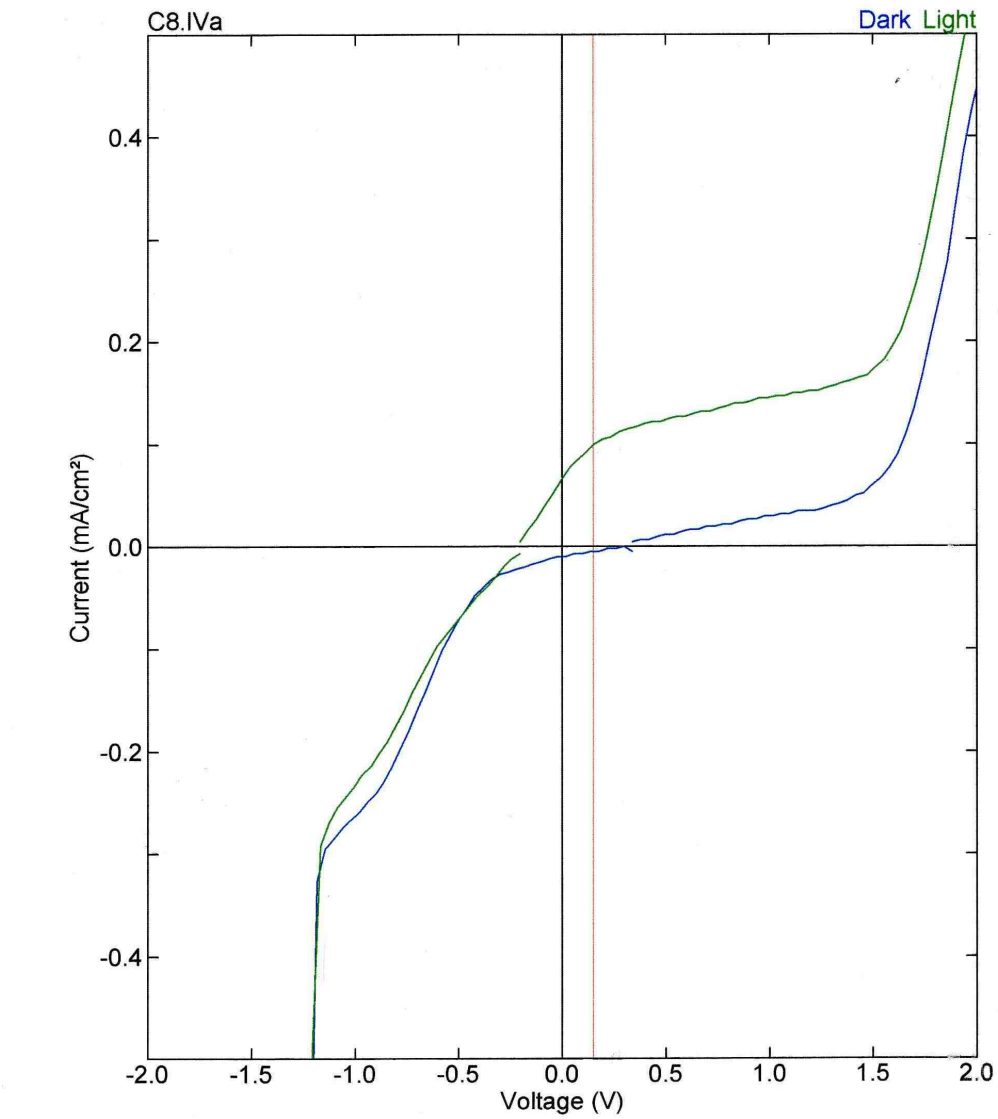

Figure 5.3: Current versus voltage curves for bulk ZnO. Illuminated (Light at 50% of the full power of UV light intensity) and without illumination (Dark)

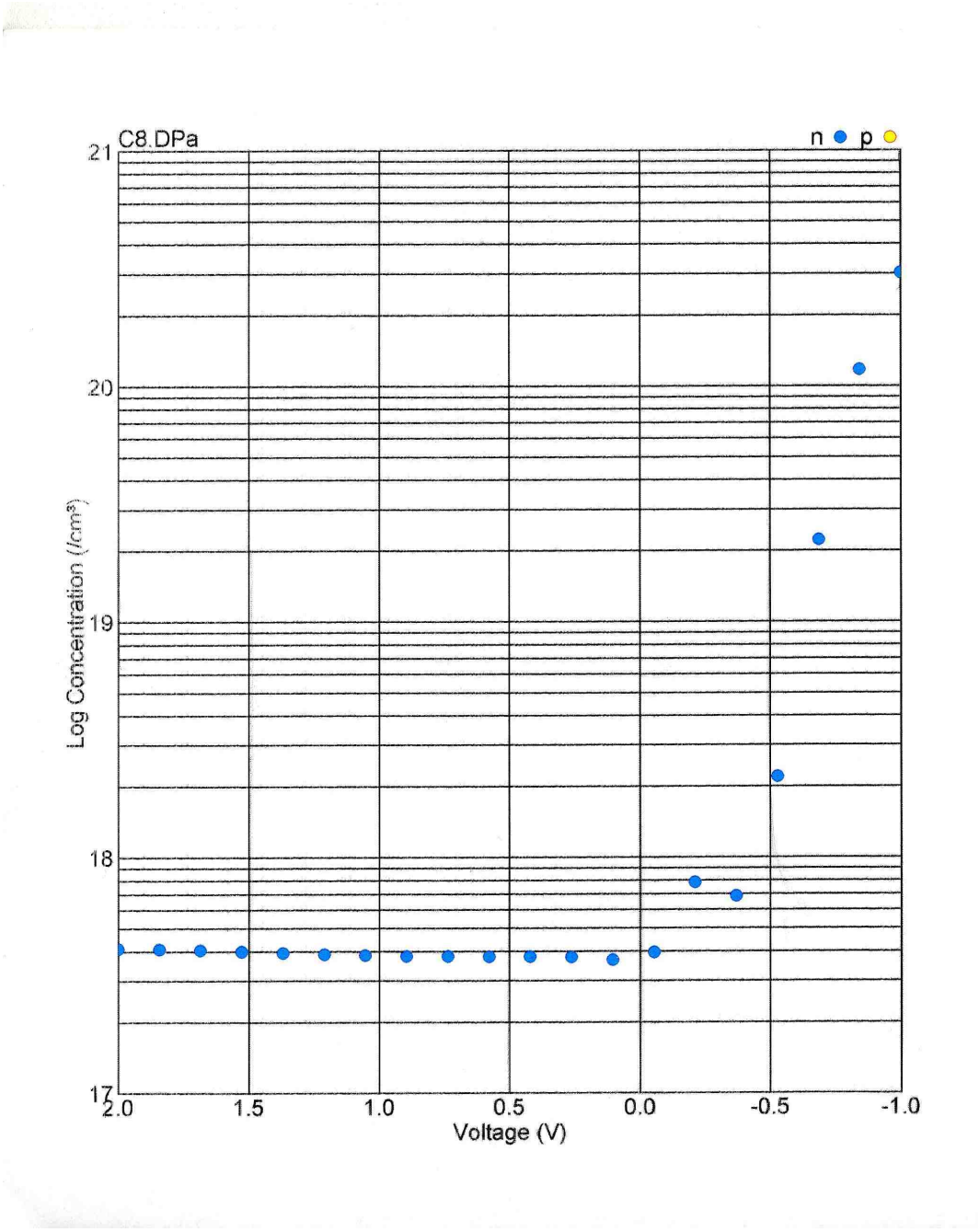

Figure 5.4: Carrier concentration versus voltage along the depletion region formed in the interface of the bulk ZnO and the electrolyte.

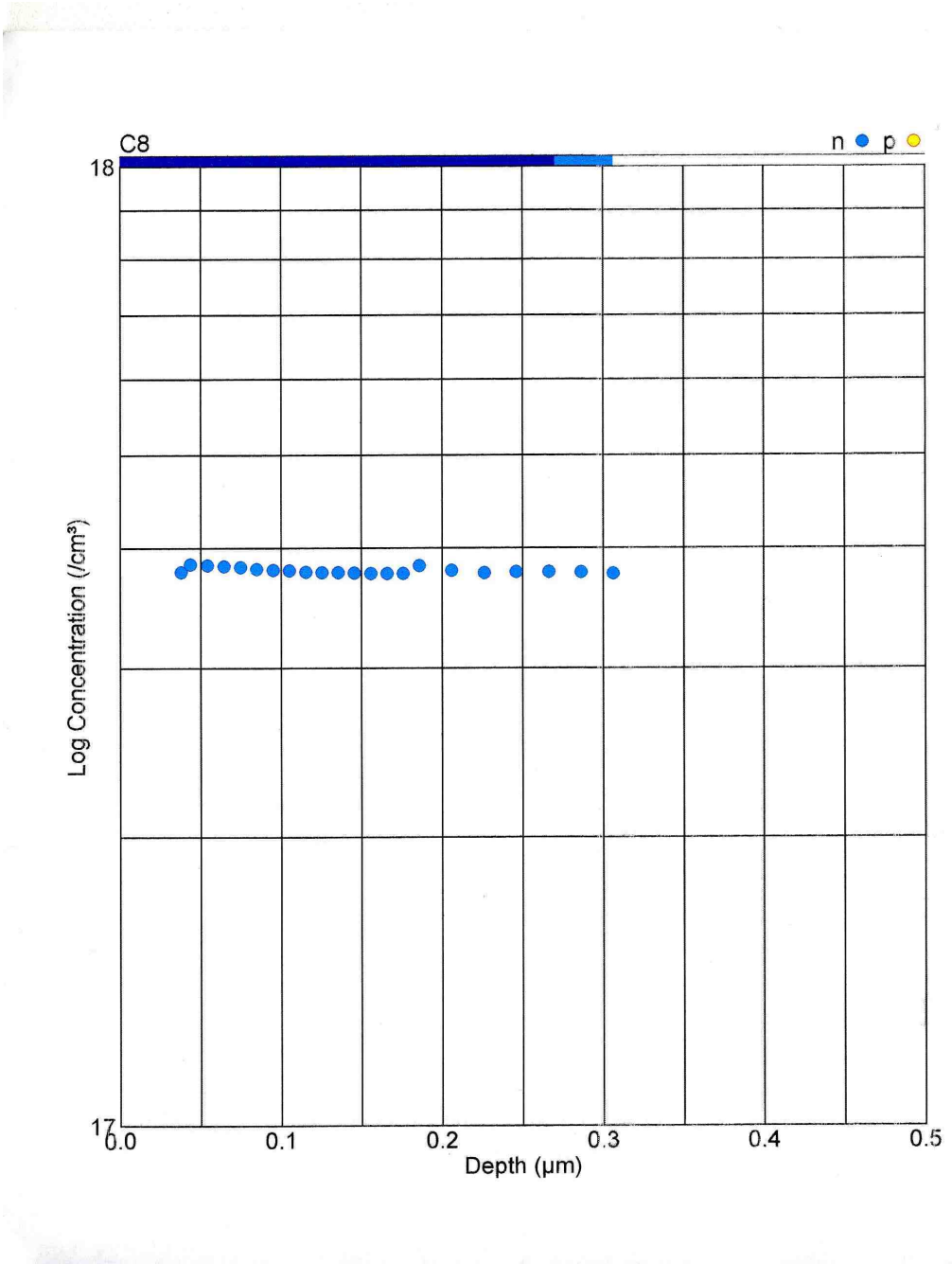

Figure 5.5: Carrier concentration profile for the ZnO etched with 0.1M $ZnCl_2$

Chapter 6

Conclusions

ZnO micro and nanostructures were grown at low temperature and atmospheric pressure under the Vapor Phase mechanism. Using SEM images obtained by collaborators we were able to determine the morphology and growth habit.

The morphology of the ZnO structures is mostly influenced by the gas-phase supersaturation and the surface energy of the growing surface planes. The vapor concentration of zinc (supersaturation) is influenced by the carrier gas flowing during the growth, defining the amount of zinc that will be deposited on the substrate. The distance from the source material also influences the supersaturation. The surface energy of different planes will define the morphology of the structures under controlled growth conditions.

The optimization of the growth is primarily controled by the temperature. Temperature influences in the reaction at the beginning of the growth process. At low temperature (from 500 to 525 °C) the condensation of small Zn droplets takes place which favors continued growth of the structures on the substrate through reaction with the ambient oxygen. The shape of the structures is mostly directed by the surface energy of the growth planes. At higher temperatures, more than 600 °C, the production of zinc vapor occurs rapidly and the reaction of zinc with oxygen occurs

in the vapor phase. In addition to nucleation on the substrate the vapor-oxygen reactants precipitated as a snowy agglomerate. A simple thermodynamic model is able to describe most but not all of the growth features observed.

The low temperature photoluminescence spectral features observed at 3.360 eV can be associated with excitons bound to the common group III impurities Al and/or Ga. The 3.356-eV line may represent an exciton bound to In, or it may be an acceptor-bound exciton, or it may be a defect-related surface feature. The 3.366-eV line is likely caused by surface states. Green luminescence is also observed. Due to the variation of its intensity with oxygen partial pressure, our samples do not indicate that the oxygen vacancy is the primary source for this band.

The electrochemical capacitance voltage technique was succesfully applied to bulk ZnO, demonstrating the accuracy in the determination of the carrier concentration. However, good Ohmic contact formation must be develop for thinner or nanostructured systems in order to perform the measurements.

Bibliography

[1] J. G. Lu, Z. Z. Ye, Y. Z. Zhang, Q. L. Liang, Z. L. Wang, and Sz. Fujita, *Appl.Phys. Lett.* **89**, 023122 (2006).

[2] Z.L.Wang, *J.Phys.:Condens.Matter* **16**, R829-R858 (2004).

[3] Y. W. Heo et al., *Appl.Phys.Lett* **85**, 2002 (2004).

[4] Y. B. Li, Y. Bando, and D. Golberg, *Appl.Phys.Lett* **84**, 3603 (2004).

[5] Y. Li, G. S. Cheng, and L. D. Zhang, *J.Mater.Res* **15**, 2305 (2000).

[6] B. B. Lakshmi, P. K. Dorhout, and C. R. Martin, *Chem.Mater* **9**, 857 (1997).

[7] J. G. Lu, Y. Z. Zhang, Z. Z. Ye, L. P. Zhu, L. Wang, B. H. Zhao, and Q. L. Liang, *Appl.Phys.Lett* **88**, 222114 (2006).

[8] D. C. Look, "New Developments in ZnO Materials and Devices", Proc. of SPIE Vol.6474, 647402(2007).

[9] D. C. Look, *J.Elect.Mat.* **35**, 1299-1305 (2007).

[10] D. C. Look, D. C. Reynolds, C. W. Litton, R. L. Jones, D. B. Eason, and G. Cantwell, *Appl.Phys.Lett.* **81**, 1830-1832 (2002).

[11] S. J. Pearton, D. P. Norton, K. Ip, Y. W. Heo, and Y. Steiner, *Prog.Mat.Sci.* **50**, 293-340 (2005).

[12] B. K. Meyer, H. Alves,D. M. Hofmann, W. Kriegseis, D. Forster, F. Bertram, J. Christen, A. Hoffman, M. Straburg, M. Dworzak, U. Haboeck and A. V. Rodina, *Phys.Stat.Sol.(b)* **241**, 231-260 (2004).

[13] J. C. Phillips, *Bonds and Bands in semiconductors*. Academic New York, 1973.

[14] U. Ozgur,Ya. I. Alivov,C. Liu,A. Teke,M. A. Reshchikov,S. Dogan,V. Avrutin,S-J. Cho, and H. Morkoc, *J.Appl.Phys* **98**, 041301 (2005).

[15] D.C.Look, B. Claflin, Y. I. Alivov, and S. J. Park, *Phys.Stat.Sol.(a)* **201**, 2203 (2004).

[16] C. G. Van de Walle, *Phys.Rev.Lett.* **85**, 1012(2000).

[17] B. P. Zhang, N. T. Binh, Y. Segawa, K. Wakatsuki, and N. Usami, *Appl.Phys.Lett* **83**, 1635 (2003).

[18] D. C. Look, B. Claflin, *Phys.Stat.Sol.(b)* **241**, 624 (2004).

[19] B. Xiang, P. Wang, X. Zhang, S. A. Dayeh, D. P. R. Aplin, C. Soci, D. Yu, and D. Wang, *NanoLetters* **7**, 323-328 (2007).

[20] Y. R. Ryu, T. S. Lee, J. A. Lubguban, H. W. White, B. J. Kim, Y. S. Park, and C. J. Youn, *Appl.Phys.Lett.* **88**, 241108 (2006).

[21] Y. R. Ryu and H. White, *Compound Semiconductor* **12**, 16-18 (2006).

[22] J. Y. Park, Y. S. Yun, Y. S. Hong, H. Oh, J. J. Kim, and S. S. Kim, *Composites:Part B* **37**, 408-412 (2006).

[23] M. S. Arnold, P. Avouris, Z. W. Pan, and Z. L. Wang, *J.Phys.Chem.B* **107**, 659-663 (2003).

[24] Ch. Pandis, N. Brilis, E. Bourithis, D. Tsamakis, H. Ali, S. Krishnamoorthy, A. Iliadis, and M. Kompitsas, *IEEE Sensors Journal* **7**, 448 (2007).

[25] F. Moreira, M. E. Hakiki, F. Sarry, L. L. Brizoual, O. Elmazria, and P. Alnot, *IEEE Sensors Journal* **7**, 336 (2007).

[26] Z. L. Wang and J. Song *Science* **312**, 242-245 (2006).

[27] Y. N. Xia, P. D. Yang, Y. G. Sun, Y. Y. Wu, B. Mayers, B. Gates, Y. D. Yin, F. Kim, and H. Q. Yan, *Adv. Mater.* **15**, 353 (2003).

[28] H. Barry Bebb and E. W. Williams *Transport and Optical Phenomena, Vol.8. in Semiconductors and Semimetals*, Ed., R. K. Willardson, A. C. Beer (Academic Press, Inc.,N.Y., 1972).

[29] J. I. Pankove, *Optical Processes in Semiconductors* (Dover Publications, Inc.,N.Y., 1971).

[30] David C. Look, *Electrical characterization of GaAs and devices* (Chichester; Wiley, New York, 1989).

[31] P. Blood, *Semicond.Sci.Technol.* **1**, 7-27 (1986).

[32] D. K. Schroder, *Semiconductors material and device characterization- 2nd edition* (John Wiley and Sons,Inc, New York, 1998).

[33] I. Barin, *Thermochemical data of Pure substances- 3rd Edition. Vol II*(Weinheim, New York, 1995).

[34] J. C. Brice, *The Growth of Crystals from the Melt, Vol. V in Selected Topics in Solid State Physics*, Ed., E. P. Wohlfarth (North-Holland Publishing Co-Amsterdam, 1965).

[35] C. Ye, X. Fang, Y. Hao, X. Teng, and L. Zhang, *J.Phys.Chem.B* **109**, 19758-19765 (2005).

[36] W. Cheng, P. Wu, X. Zou and T. Xiao, *J.Appl.Phys* **100**, 054311 (2006).

[37] W. J. Li, E. W. Shi, W. Z. Zhong, and Z. W. Yin, *J.Crys.Growth* **203**, 186-196 (1999).

[38] R. C. Wang, C. P. Liu, J. L. Huang, S. J. Chen, Y. K. Tseng and S. C. Kung, *Appl.Phys.Lett* **87**, 013110 (2005).

[39] L. Wang and N.C.Giles, *J.Appl.Phys* **94**, 973 (2003).

[40] A. B. Djurišić, W. M. Kwok, W. K. Chan, D. L. Phillips, Y. H. Leung, M. H. Xie, H. Y. Chen, C. L. Wu and S. Gwo, *J.Appl.Phys* **99**, 033517 (2006).

[41] D. C. Reynolds, D. C. Look, B. Jogai, C. W. Litton, T. C. Collins, W. Harsch, and G. Cantwell, *Phys.Rev.B* **57**, 12151-12155 (1998).

[42] D. C. Reynolds, C. W. Litton, and T. C. Collins, *Phys.Rev* **140**, A1726 (1965).

[43] J. Gutowski, N. Presser, and I. Broser, *Phys.Rev.B* **38**, 9746 (1988).

[44] V. A. Fonoberov, K. A. Alim, A. A. Balandin, F. Xiu, and J. Liu, *Phys.Rev.B* **73**, 165317 (2006).

[45] S. Müller, D. Stichtenoth, M. Uhrmacher, H. Hofsäs, and C. Ronning, *Appl.Phys.Lett* **90**, 012107 (2007).

[46] K. Johnston, M. O. Henry, D. McCabe, E. McGlynn, M. Dietrich, E. Alves, and M. Xia *Phys.Rev.B* **73**, 165212 (2006).

[47] T. Makino, A. Tsukazaki, A. Ohtomo, M. Kawasaki, and H. Koinuma, *Jpn.J.Appl.Phys* **45**, 6346-6351 (2006).

[48] G. Xiong, K. B. Ucer, R. T. Williams, J. Lee, D. Bhattacharyya, J. Metson, and P. Evans, *J.Appl.Phys* **97**, 043528 (2005).

[49] K. Thonke, T. Gruber, N. Teofilov, R. Schönfelder, A. Waag, and R. Sauer, *Physica B* **308-310**, 945-948 (2001).

[50] S. B. Zhang, S. H. Wei, and A. Zunger, *Phys.Rev.B* **63**, 075205 (2001).

[51] R. Dingle, *Phys.Rev.Lett.* **23**, 579 (1969).

[52] N. C. Giles, Y. Jiang, X. Yang, S. M. Evans, and L. E. Hallinburton *Mater. Res. Soc. Symp. Proc.* **957**, 0957-K03-04 (2007).

[53] S. A. Studenikin, N. Golego, and M. Cocivera, *J.Appl.Phys.* **84**, 2287 (1998).

[54] A. B. Djurišić, Y. H. Leung, K. H. Tam, L. Ding, W. K. Ge, H. Y. Chen, and S. Gwo, *Appl.Phys.Lett* **88**, 103107 (2006).

[55] A. F. Kohan, G. Ceder, D. Morgan, and C. G. Van de Walle, *Phys.Rev.B* **61**, 15 019 (2001).

[56] P. Schröer, P. Krüger, and J. Pollmann, *Phys.Rev.B* **47**, 6971 (1993).

[57] E. Rauls and Th. Frauenheim, *Phys.Rev.B* **69**, 155213 (2004).

[58] F. W. Sears, G. L. Salinger, *Thermodynamics, Kinetic Theory, and Statistical Thermodynamics- 3rd Edition* (Addison-Wesley Publishing Company, 1975).

[59] J. G. Lu, Z. Z. Ye, J. Y. Huang, L. P. Zhu, B. H. Zhao, Z. L. Wang, and Sz. Fujita, *Appl.Phys.Lett.* **88**, 063110 (2006).

[60] X. Tang, A. Clauzonnier, H. I. Campbell, K. A. Prior, and B. C. Cavenett, *Phys.Stat.Sol.(c)* **1**, 860-863 (2004).

[61] P. Chang, Z. Fan, D. Wang, W. Tseng, W. Chiou, J. Hong and J. G. Lu, *Chem.Mater.* **16**, 5133-5137 (2004).

[62] Y. Li, M. Feneberg, A. Reiser, M. Schirra, R. Enchelmaier, A. Ladenburger, A. Langlois, R. Sauer, K. Thonke, J. Cai, and H. Rauscher, *J.Appl.Phys* **99**, 054307 (2006).

[63] Y. Gu, I. L. Kuskovsky, M. Yin, S. O'Brien, and G. F. Neumark, *Appl.Phys.Lett.***85**, 3833 (2004).

[64] C. E. Stutz, *J.Electron.Mater.* **30**, L40-L42 (2001).

[65] *PN4300 Electrochemical C-V Profiler with Photovoltage Spectroscopy. User Manual* 94300PUM01 Issue 4.0.

[66] Cermet, Inc., 1019 Collier RD, Suite C-1, Atlanta, GA 30318.

[67] J. Nause and B. Nemeth, *Semicond. Sci. Technol.***20**, S45-S48 (2005).